Supplementary information

Spinel Oxide Enables High-Temperature Self-Lubrication in Superalloys

Zhengyu Zhang[a], Eitan Hershkovitz[b], Qi An[c], Liping Liu[d], Xiaoqing Wang[e], Zhifei Deng[f], Garrett Baucom[b], Wenbo Wang[a], Jing Zhao[g], Ziming Xin[a], Lowell Moore[g], Yao Yi[h], Md Rezwan Ul Islam[i], Xin Chen[i], Bai Cui[i], Ling Li[f], Hongliang Xin[d], Lin Li[h,*], Honggyu Kim[b,*], and Wenjun Cai[a,*]

a. Department of Materials Science and Engineering, Virginia Polytechnic Institute and State University, Blacksburg VA, 24061, United States
b. Department of Materials Science and Engineering, University of Florida, Gainesville, FL 32603
c. Department of Materials Science and Engineering, Iowa State University, Ames, IA 50011
d. Department of Chemical Engineering, Virginia Polytechnic Institute and State University, Blacksburg VA, 24061, United States
e. Department of Applied Engineering, Jacksonville State University, Jacksonville AL 36265, United States
f. Department of Mechanical Engineering, Virginia Polytechnic Institute and State University, Blacksburg VA, 24061, United States
g. Department of Geosciences, Virginia Polytechnic Institute and State University, Blacksburg VA, 24061, United States
h. School for Engineering of Matter, Transport and Energy, Arizona State University, Tempe, AZ, 85287, United States
i. Department of Mechanical and Materials Engineering, University of Nebraska-Lincoln, Lincoln, NE, 68588, United States

* Corresponding authors' email address: lin.li.10@asu.edu (L. Li), honggyukim@ufl.edu (H. Kim), caiw@vt.edu (W. Cai).

Contents

1. Alloy manufacturing and heat treatment

1.1. Composition of the Inconel 718 powder

Supplementary Table 1. The chemical composition of the Inconel 718 powder (wt.%).

Fe	Ni	Cr	Nb	Mo	Ti	Al	Co	Cu	Mn	Si	Ta	C
Rem.	50-55	17-21	4.75-5.5	2.8-3.3	0.65-1.15	0.2-0.8	<1	<0.3	<0.35	<0.35	<0.05	<0.08

1.2. Phase prediction after heat treatment

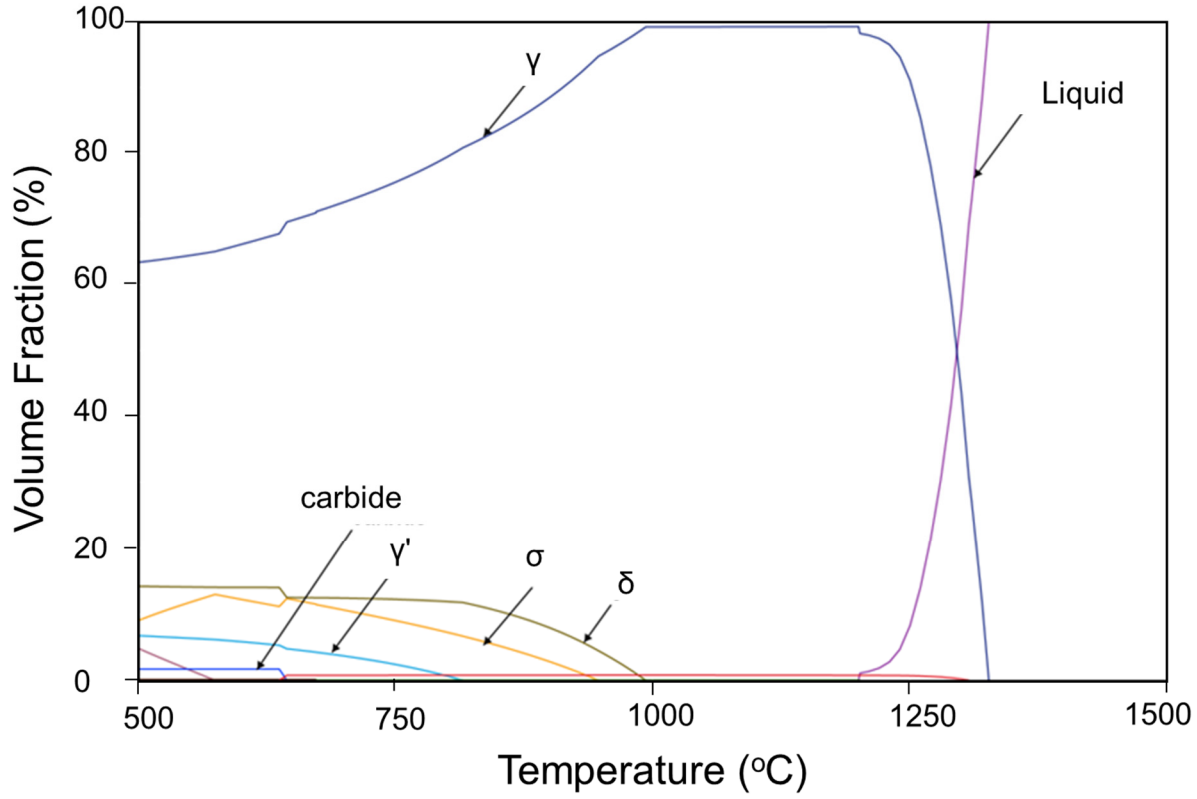

Supplementary Figure 1. Predicted phase evolution of Inconel 718 due to heat treatment. Thermo-calc software (TCNI12 database, version 2023b) was used to calculate the phase volume fraction of Inconel 718 as a function of temperature. Phases with significant volume fractions (larger than 5 vol%) are labeled. Other phases in small amount (less than 5 vol%) are not included in the plot, such as MB2_C32 carbide, BCC_B2, FCC_L12 and the intermetallic τ phase.

1.3. Microstructure of as-printed and heat-treated samples

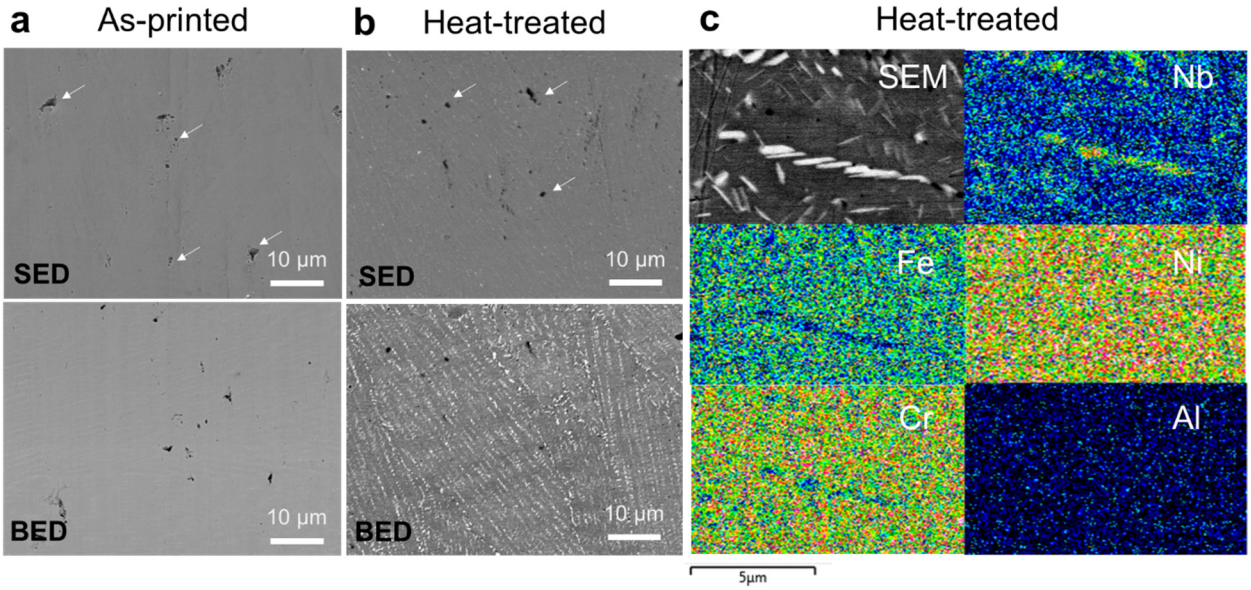

Supplementary Figure 2. Microstructure of Inconel 718 samples before wear test. Secondary electron microscopy images of **a** as-printed and **b** heat-treated Inconel 718 measured from secondary electron detector (SED) and backscattered electron detector (BED). **c** BED images and elemental maps from Energy Dispersive X-ray Spectroscopy (EDS) of heat-treated sample.

1.4. Effects of heat treatment on diffusion paths

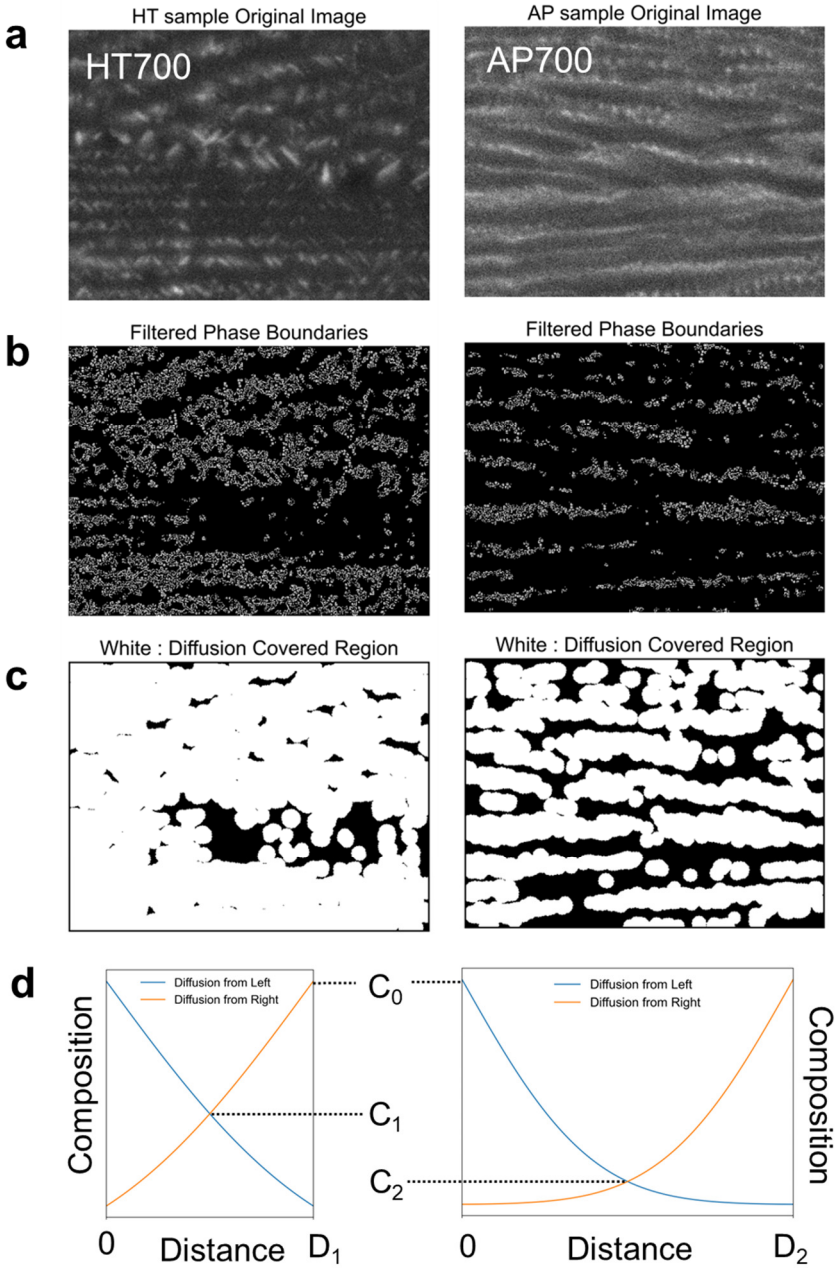

Supplementary Figure 3. Effects of heat treatment on diffusion paths for surface oxidation of AP700 and HT700. a SEM images **b** filtered phase map **c** processed phase map for diffusion areas, and **d** schematic plots of concentration profiles for HT700 (left column) and AP700 (right column) samples.

Note on Supplementary Figure 3

The region encapsulated by the white circles denote a high Cr concentration zone, with the HT sample exhibiting a more uniform distribution. Furthermore, assuming that the HT and AP samples possess average phase boundary distance of D1 and D2 respectively, where D1 is less than D2. Cr exhibit fast diffusion at phase boundaries and its bulk diffusion is neglected in this model. Given a specific time frame. the HT and AP samples will have a concentration of C_1 and C_2 at their median points along its concentration gradient, where C_1 is higher than C_2**.** This implies that the HT sample would present a more uniform Cr diffusion on its surface, precluding the formation of expansive corundum structures.

1. Initial Analysis: We initiated our study by mapping the distribution of the niobium (Nb) element across our samples (Supplementary Figure 3a). This mapping served as the preliminary input for our analysis.
2. Phase Boundary Identification: Through image filtering techniques, we isolated the phase boundaries within the samples (Supplementary Figure 3b). These boundaries are critical as they facilitate the diffusion of chromium (Cr).
3. Diffusion Region Determination: We identified the diffusion-covered regions (Supplementary Figure 3c), which are areas where Cr diffusion is notably effective.
4. Comparative Study: We observed a marked difference in the diffusion-covered regions between the HT700 and AP700 samples. This was accomplished by measuring the distance from the black points (non-boundary regions) to the nearest phase boundary.
5. Distance Measurement: Our measurements revealed that the HT700 had a more extensive coverage by phase boundaries, indicated by a shorter average distance of $D_1 = 0.133$ μm compared to the AP700 sample's average of $D_2 = 0.238$ μm.
6. Diffusion Illustration: To illustrate the process, we employed Fick's second law in a two-dimensional model. 'D_1' and 'D_2' represent the average distances between phase boundaries, with D_1 being less than D_2.
7. Concentration Assumption: For simplification, we assumed a high and constant Cr concentration (C_0) at the phase boundaries.
8. Diffusion Simulation: We then simulated Cr diffusion from both the left and right boundaries over a given time t.
9. Concentration Analysis: The schematic in Supplementary Figure 3d illustrates that the midpoint concentration for HT700 and AP700 samples will be C_1 and C_2, respectively. Notably, C_1 is significantly closer to C_0 than C_2, indicating a more uniform Cr distribution.
10. Conclusion: The analysis concludes that HT700 samples are likely to exhibit a more uniform surface distribution of Cr compared to AP700 samples, which can be attributed to the more extensive and effective phase boundary coverage. Such uniform distribution minimizes the formation of large spherical corundum structures seen in AP700. AP900, and HT900 samples.

2. High temperature hardness measurements

2.1. Procedure

Hardness tests were conducted at four temperature points (20 °C, 600 °C, 700 °C, and 800 °C) using a diamond indenter with high-temperature indentation equipment (Manufacturer: Rtec-Instrument, Model: MFT5000, Serial: RTECH3010) in an argon environment. Supplementary Figure 4 shows the photo of the machine and the test setup. The maximum achievable temperature, limited by the equipment, was 800 °C. Four indentations were made at each temperature point to determine the average hardness and standard deviation. A 30 N load was applied for 10 seconds during each indentation. Following the indentations, the samples were cooled in an argon environment. Once the samples reached room temperature, the diagonal dimensions of the indents were measured using a microscope on a separate microhardness testing device (Manufacturer: ITW Test & Measurement GmbH, Model: Tukon 2500-3):.

The Vickers Hardness (HV) was calculated using the following equations:

$$HV = constant \times \frac{test\ force\ (F)}{surface\ area\ of\ the\ indent} = 0.102 \times \frac{2Fsin\frac{136^o}{2}}{d^2} = 0.1891 \times \frac{F}{d^2}, \quad (1)$$

$$d = \frac{d_1+d_2}{2} \text{ (average diagonal length).} \quad (2)$$

The Vickers Hardness (HV) was then converted to hardness in GPa using the following equation:

$$Hardness\ (GPa) = 0.009807 \times Vickers\ Hardness\ (HV) \quad (3)$$

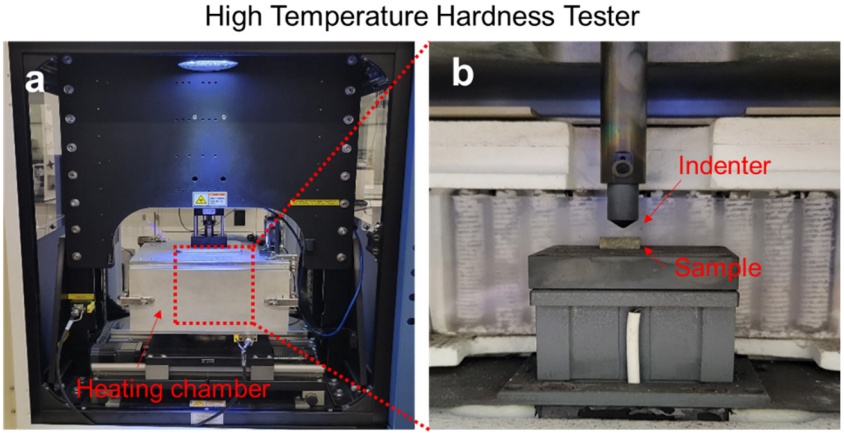

Supplementary Figure 4. High temperature indentation equipment. a Photo of the heating chamber of the indentation machine. **b** A view of the indenter and the Inconel sample.

2.2. Results

Supplementary Figure 5 presents the results for HT and AP samples, with representative indent images shown in Supplementary Figures 5b and 5c. The measurements at room temperature

align with the results shown in Section 5. At all elevated temperatures tested, the HT samples exhibited higher hardness than the AP samples.

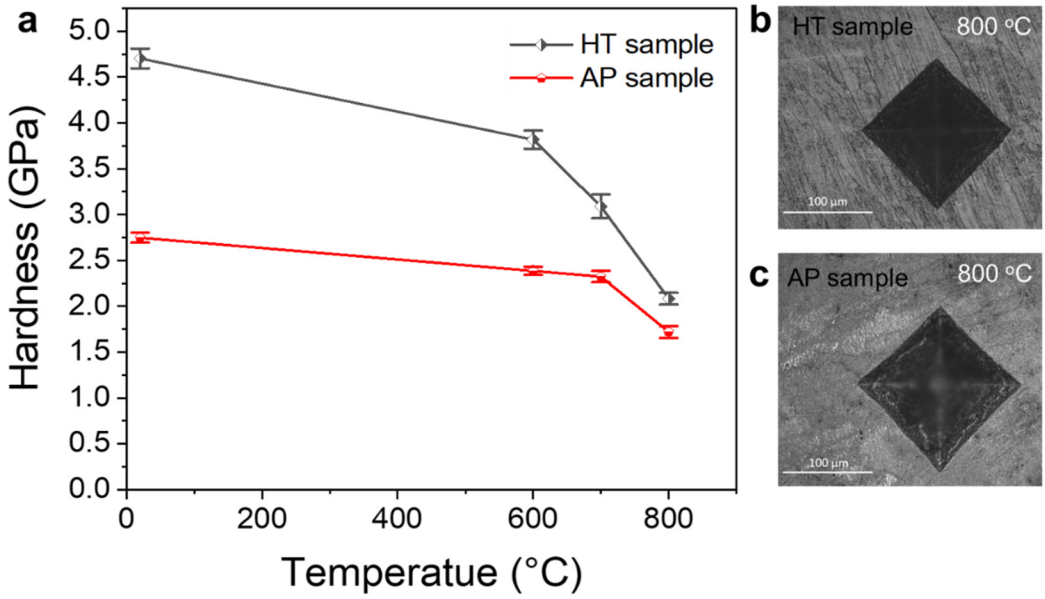

Supplementary Figure 5. a. High-temperature hardness of (unworn) as-printed (AP) and heat-treated (HT) Inconel 718 samples. Indent SEM images of b HT and c AP sample tested at 700 °C.

3. High temperature tribological tests

3.1. Test setup and validation

Supplementary Figure 6 shows the setup for the high temperature wear test, including a photo of the heating chamber and the sample mounting. To evaluate the test setup using the Rtec tribometer, we performed wear tests using stainless steel 316 coupons against Al_2O_3 ball. Tests were conducted at room temperature under ambient conditions, with a sliding speed of 20 mm/s and a Hertzian contact pressure of 1.59 GPa, replicating the conditions reported in Ref [1]. As shown in Supplementary Figure 7a**,** the COF of stainless steel 316 against Al_2O_3 ball has an average value of 0.57, which agrees well with the value (COF=0.56) reported in Ref [1].

In addition, we also evaluated the extent of how counterbody material type affect the frictional response by performing wear test under the same conditions (i.e. sliding speed, Hertizan pressure) using tungsten carbide (WC) ball as counterbody. The results in Supplementary Figure 7b shows that a lower COF (COF=0.51) was obtained using WC counterbody than that using Al_2O_3 ball (COF=0.57). Based on these observations, we limit the literature data in Fig 1h to include only those using Al_2O_3 counterbodies.

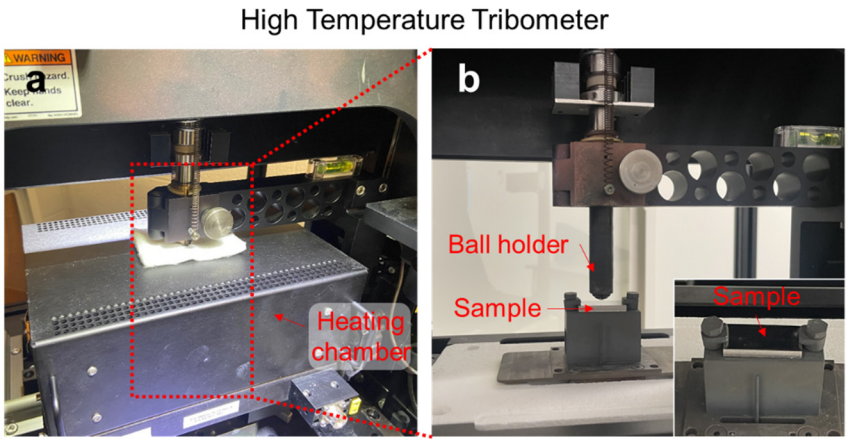

Supplementary Figure 6. Photographs of the high-temperature tribological tester (Rtec MFT-5000). a A close-up of the tester with the heating chamber installed. **b** A view of the ball holder and Inconel sample with the heating chamber removed. The inset in **b** shows a top-down view of the sample, secured by two side screws.

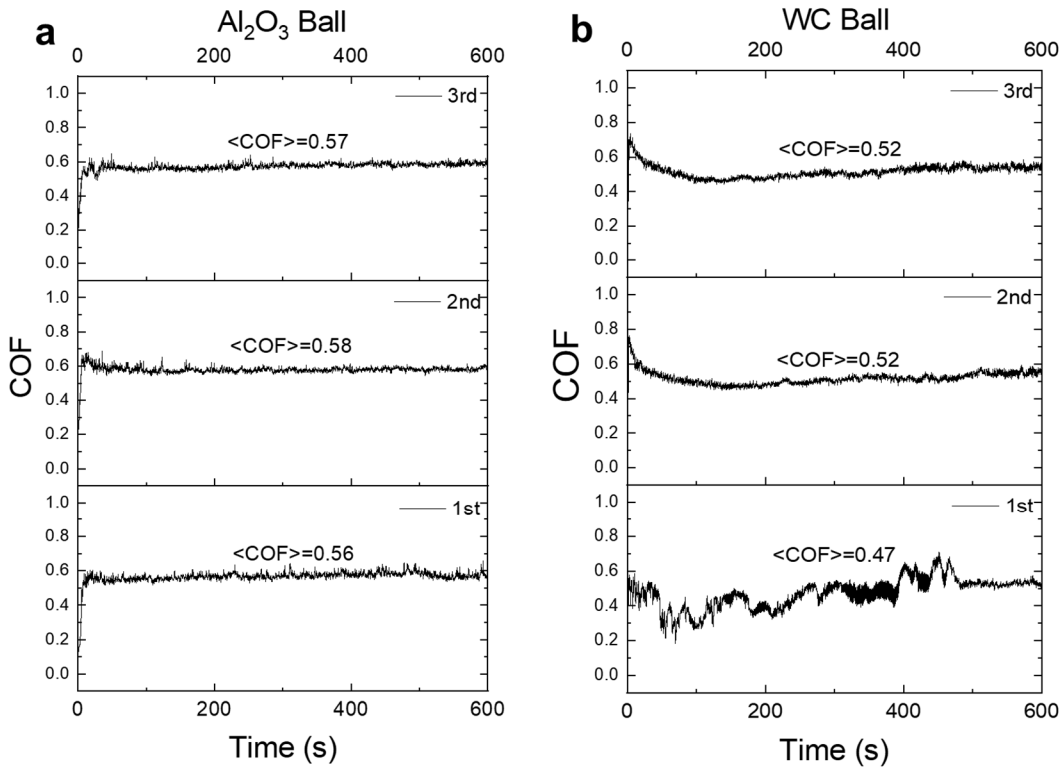

Supplementary Figure 7. Validation test results using two different counter bodies: (a) COF of stainless steel 316 against an Al_2O_3 ball and (b) COF against a WC ball. Tests were conducted at room temperature under ambient conditions, with a sliding speed of 20 mm/s and a Hertzian contact pressure of 1.59 GPa, replicating the conditions reported in Ref [1]. COF values presented in this figure are obtained after processing via RTECviewer software. See supplementary information section 3.3 for details.

3.2. List of references used in Figure 1h

A literature survey was performed on the COF values reported so far for metals from room temperature to 1000 ºC are obtained from the following references: [2, 3, 4, 5, 6, 7, 8, 9, 10, 11, 12, 13, 14, 15, 16, 17, 18, 19, 20, 21, 22, 23, 24, 25, 26, 27, 28, 29, 30, 31, 32, 33, 34, 35, 36, 37, 38, 39, 40, 41, 42]. Among these reports, data from those using Al_2O_3 as counterbody was plotted in Figure 1h.i of the paper (see second tab of the Source Data for the paper titles). The raw data from this literature review is provided in the Source Data.

3.3. Raw vs. processed data

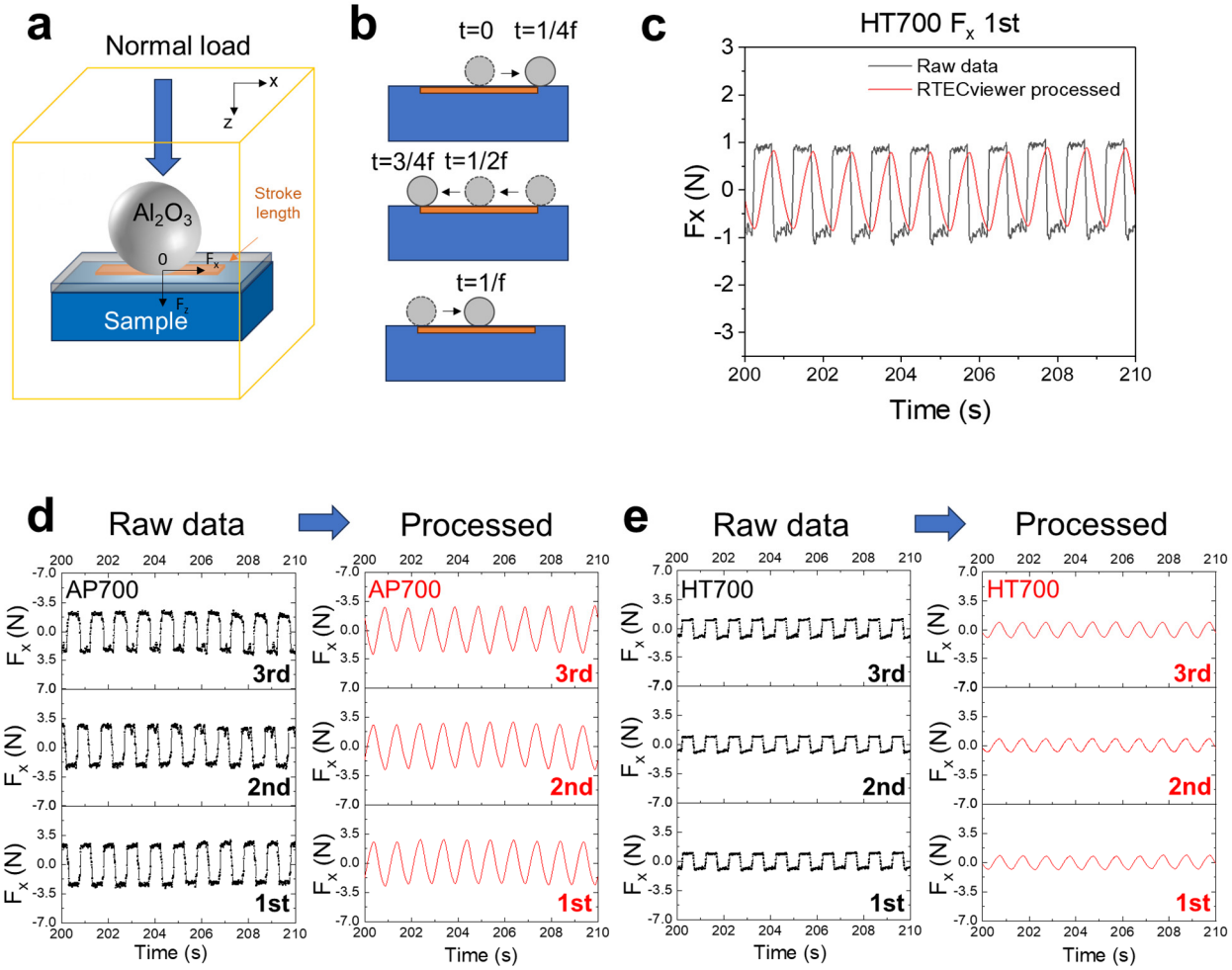

Supplementary Figure 8. Comparison of raw and processed data. a Schematic of the reciprocal motion between the ball and the Inconel sample. **b** Schematic showing the ball's position on the sample as a function of time, with f representing the testing frequency. **c** Example of raw versus RTECviewer software-processed COF data for the HT700 sample from 200 to 210 seconds. Examples of raw versus RTECviewer software-processed friction force (F_x, as defined in **a**) for the **d** AP700 and **e** HT700 samples from 200 to 210 seconds. The total duration of the wear test for both samples is 600 seconds. 1st, 2nd, and 3 rd represents three repeated tests.

In reciprocal wear, it is important to understand that for a test conducted at a frequency of f, the period for the ball to move back and forth once and return to its initial position will take a time of 1/f, as illuastrated in Supplementary Figure 8a,b. In this work, f = 1 Hz, so that the period is 1 sec. Thus the raw data of F_x (frictional force) fluctuates between a positive and negative value when the ball swithches direction in the reciprocal motion, resemebling a square waveform, as shown in Supplementary Figure 8d,e. Supplemantery Figure 9 and 10 show such oscilation of the normal (F_z) and frictional force (F_x) due to this cyclic motion for AP700 and HT700 samples from three repeated tests.

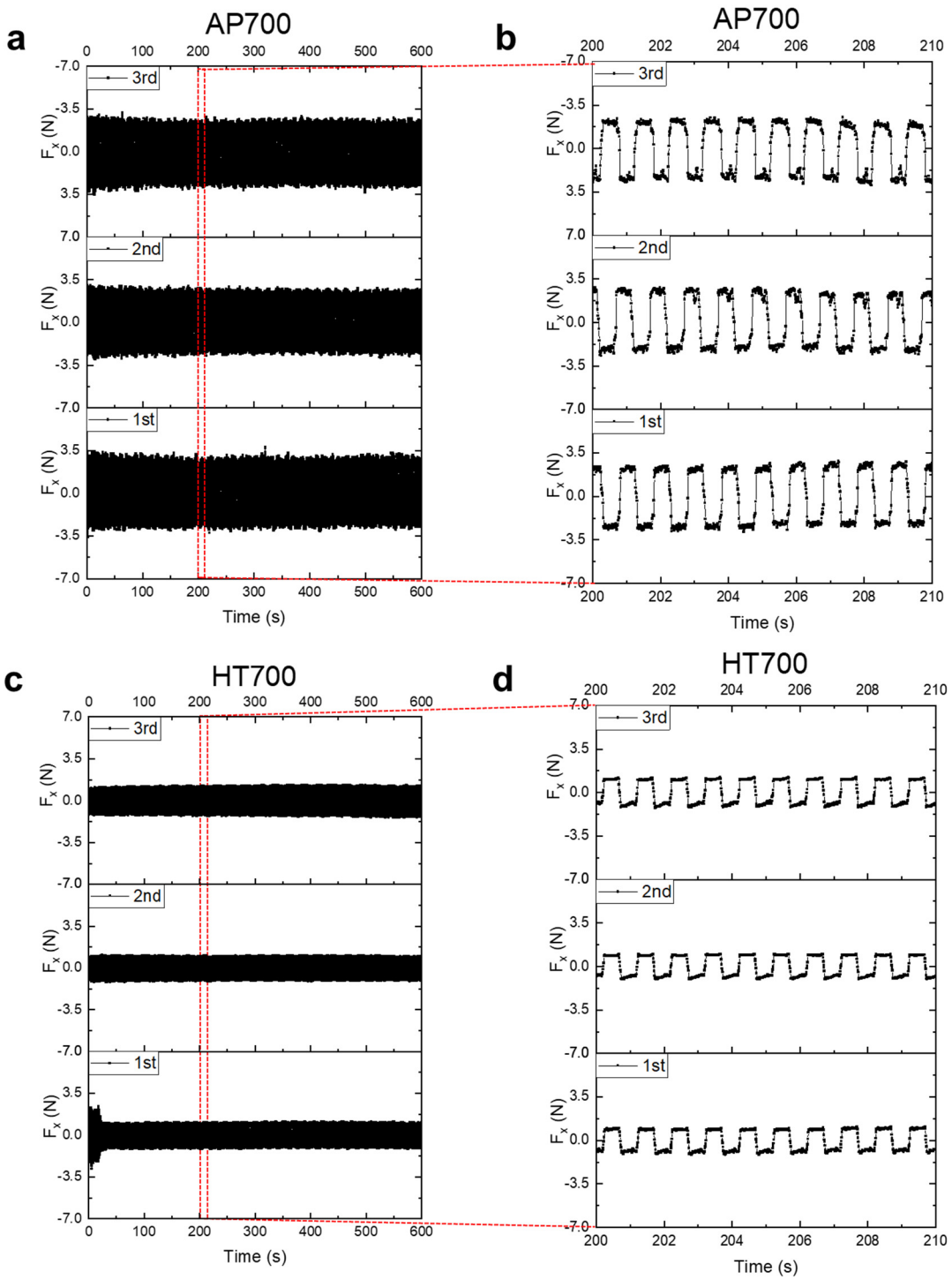

Supplementary Figure 9. Raw data of the frictional force (F_x). a,c Raw data (not processed by the RTECviewer software) of frictional force (F_x, as defined in **Supplementary Figure 8a**) of AP700 and HT700. F_x from 200 to 210 seconds of **b** AP700 and **d** HT700 sample. 1st, 2nd, and 3rd represent three repeated tests.

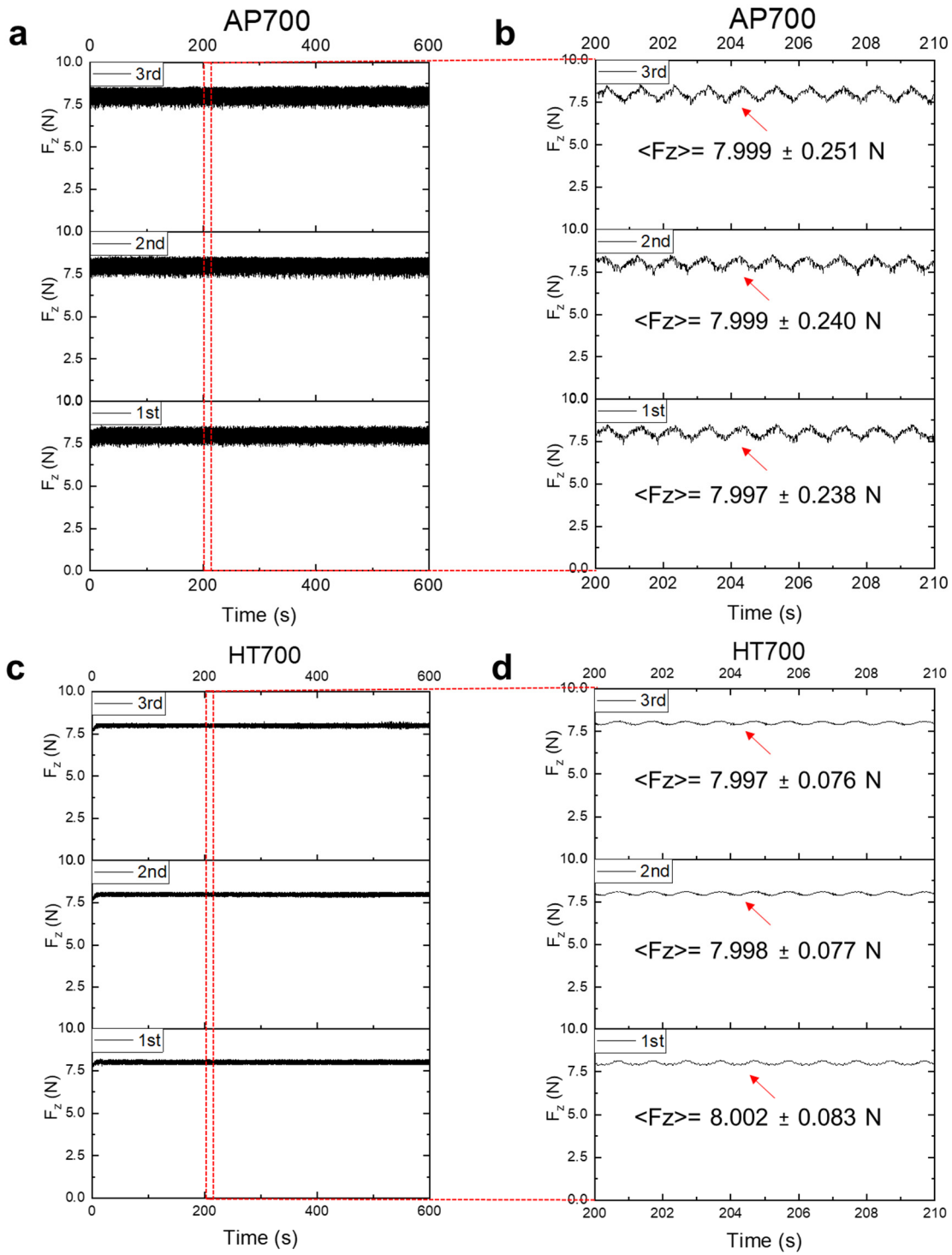

Supplementary Figure 10. Raw data of the frictional force (F_z). a,c Raw data (not processed by the RTECviewer software) of normal force (F_z, as defined in **Supplementary Figure 8a**) of AP700 and HT700. F_z from 200 to 210 seconds of **b** AP700 and **d** HT700 sample. Values in **< >** from **b, d** represent average values of F_z from the entire test (600 sec). 1st, 2nd, and 3 rd represents three repeated tests.

Using such raw data, COF (defined as the absolute value of F_x/F_z) of all samples are obtained, as shown in Supplementary Figure 11. A closer examination shows that there is significant fluctuation of the COF values due to COF becoming very close to zero every time the motion changes direction, i.e. every 0.5 sec, as shown in Supplementary Figure 12.

For such raw data, the default processing by the RTECviewer software (Version 1.4) is to perform the following treatment of F_x, F_z, and COF mathematically to minimize the effects of these near-zero values. For example, the force (F_x or F_z) at time t is processed as:

$$Force\_t\_mean = \frac{\int_{t-\delta t}^{t} Force\_t \times dt}{\delta t},\ \delta t = \frac{1}{2f} = 0.5\ sec. \quad (4)$$

where *Force_t* is the raw data of force at time *t*, and *Force_t_mean* is the software processed force at time *t*.

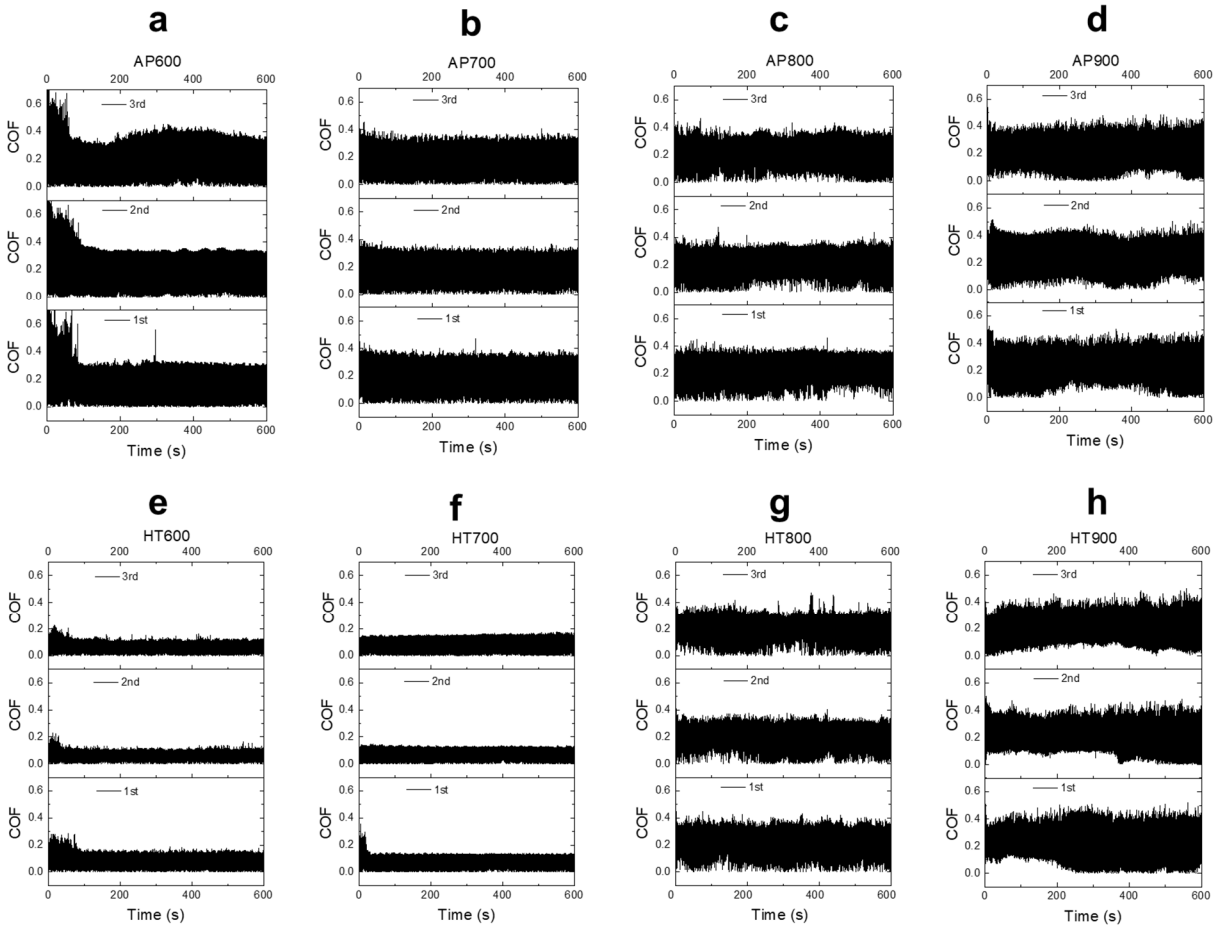

Supplementary Figure 11. Raw data of COF. a,c Raw data (not processed by the RTECviewer software) of COF of **a** AP600, **b** AP700, **c** P800, **d** AP900, **e** HT600**, f** HT700, **g** HT800, and **h** HT900. 1st, 2nd, and 3rd represent three repeated tests.

Supplementary Figure 12 shows that such processed data smooths the raw COF curve for AP700. However, for HT700, whose raw COF shows little fluctuation, the amplitude of processed data is even higher than the original raw data. For example, Supplementary Figure 13b-c shows

that the amplitude of processed data is lower than raw data for AP700, AP900, and HT900 sample, but is higher than raw data for HT700. We also performed an analysis to evaluate whether such treatment affects the average value of COF. As shown in Supplementary Figure 13a, the difference between average COF between the raw and processed data is negligible for most samples (i.e. AP700, AP800, AP900, HT800, and HT900). However, it becomes noticeable for AP600, HT600, and HT700, likely due to their relatively higher COF during the running-in (see the first ~ 50 -100 sec of Supplementary Figure 11a,e, and f) than that of the steady-state period, which caused the COF of the processed data to be slightly higher than that of the raw data. For this reason, only raw data is used in Figures 1 and 2 of the main text, including F_x, F_z, and COF. The COF values, including the average and standard deviation from the raw data, are summarized in Table R1 below.

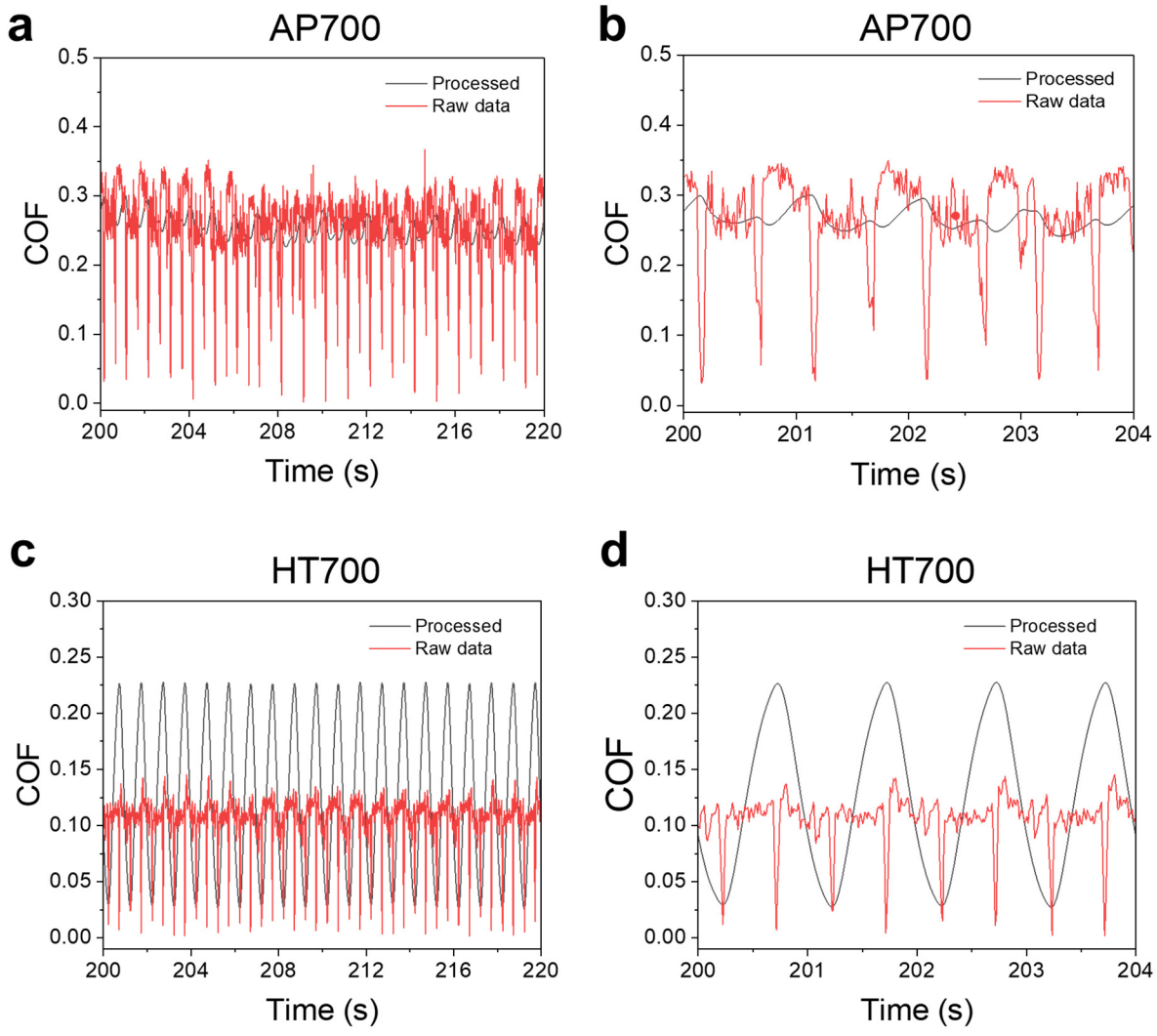

Supplementary Figure 12. Raw vs. processed data of COF. a,c Raw vs. processed COF data by the RTECviewer software of **a,b** AP700, and **c**,**d** HT700 near 200 sec.

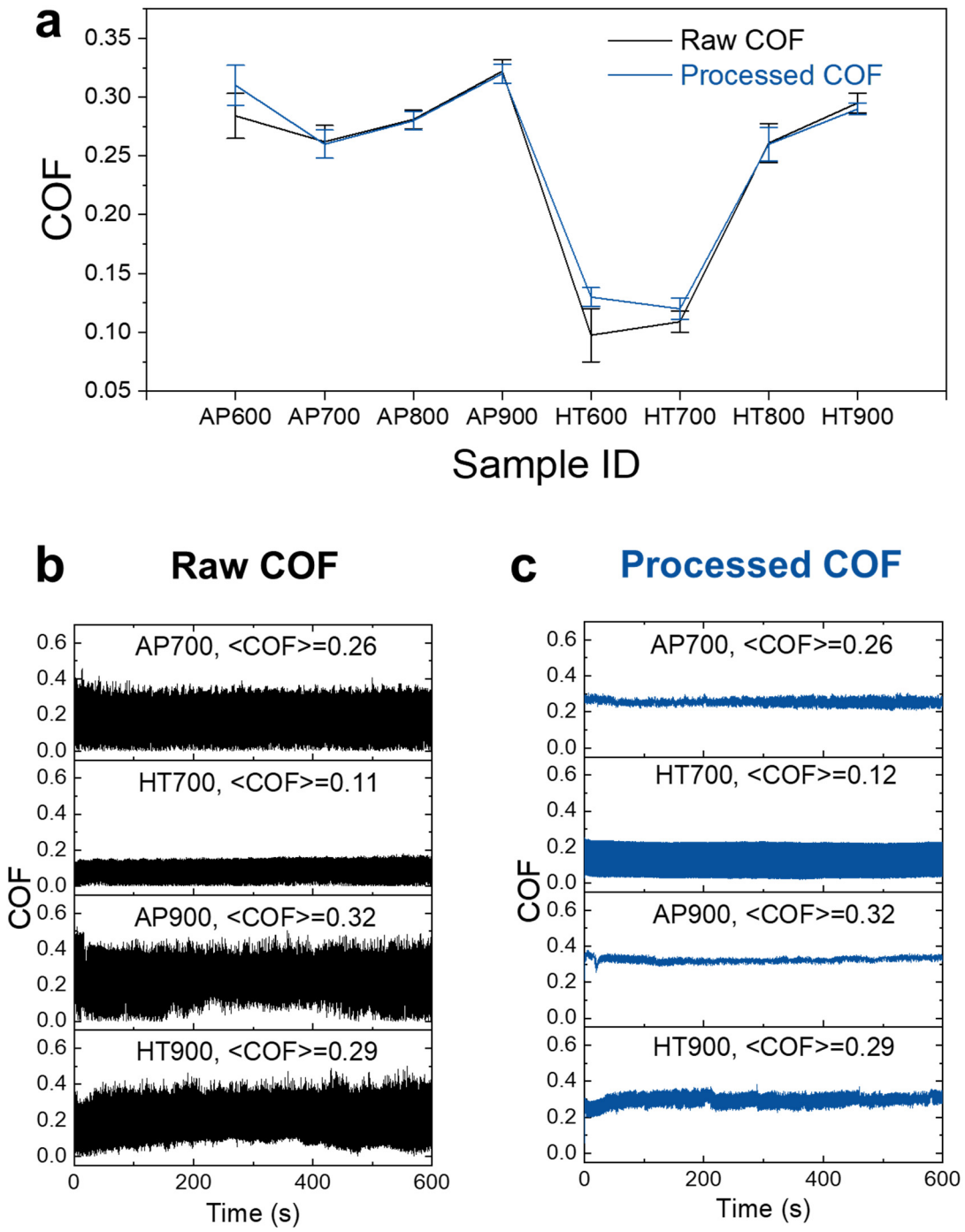

Supplementary Figure 13. Comparison of COF from raw vs. processed data. a Average COF from raw vs. processed data by the RTECviewer software for all samples. **b** Raw and **c** processed COF data for AP700, HT700, AP900, and HT900 samples.

Supplementary Table 2. Summary of average and standard deviation of raw COF data. <COF> represents the average value while SD represents the standard deviation. The raw data used to generate this table is provided in the Source Data.

Temperature (°C)	HT		AP	
	<COF>	SD	<COF>	SD
600	0.0976	0.0226	0.284	0.0191
700	0.109	0.009	0.262	0.0139
800	0.261	0.0163	0.281	0.008
900	0.295	0.00859	0.322	0.01

3.4.Power spectrum of COF

Supplementary Figure 14 shows the power spectrum of raw COF data for the 700 °C and 900 °C wear tests. Typically, in dry sliding wear with stick-slip, the self-organized criticality in COF results in a linear relationship in its power spectrum [43, 44, 45]. This is indeed observed in AP700, AP900 and HT900 samples. However, the HT700 sample's COF(t) power spectrum exhibits large fluctuations from 0.1 Hz (10^{-1} Hz) to 1 Hz (10^{0} Hz) that deviates from the linear slope of the higher frequencies (above 1 Hz), suggesting the presence of an instability in this system, which could possibly be due to phase transitions between the cubic and tetragonal spinel phases in the surface oxide layer. Previously, Yu et al. [46] reported similar breakdown of COF power law due to phase transformation and structural relaxation in metallic glass.

In Supplementary Figure 14 and 15, it is also noted that in the power spectrum of the wear tests performed at 1 Hz, prominent peaks at and above 1 Hz reflects the test itself. Similar patterns can be found in the literature [47, 48], where the lowest frequency sharp peak precisely corresponds to sample spinning, the subsequent peaks being its harmonics. Additionally, the 1/f noise was identified as a low frequency pattern below 0.01 Hz [48]. Therefore, to investigate wear-driven phase transition, we focus on frequencies in the 0.1-1 Hz range, potentially driven by the reciprocal movement. At a given location on the wear track, if the phase transition is driven by the sliding wear at 1 Hz, we assume that such phase transition at this location have a period larger than 1 second (1/f). Phase transitions could manifest in various modes with different periods. First, partial phase transitions within 1 second may result in total transfer frequencies lower than 1 Hz. Second, location on the wear track influences the transition periods. The center point in the stroke length experiences scratching every 0.5 seconds, while edge points may encounter 0.1-second and 0.9-second intervals (see Supplementary Figure 8a-b). For these reasons, the 0.1-1 Hz range power spectra should be most relevant regarding the phase transitions.

From an energy perspective, both stick-slip and phase transitions occur at energetically favorable points. Stick-slip happened at shorter times, while phase transitions (e.g., between spinel and corundum phases or between high and low symmetry spinel phases) on the wear track is driven by the sliding frequency, which is 1 Hz in the current work. Thus, phase transition is expected to occur at lower than 1 Hz frequencies while stick-slip at higher than 1 Hz frequencies. In other words, the stick-slip and phase transition events likely coexist, but in different frequency domains.

Given that a stress of 3.88 GPa is enough for spinel-corundum transition and 0.5 GPa is enough for the Jahn-Teller effect at ideal situation from DFT calculations, the above phase transitions could occur during the wear test.

To better investigate the influence of wear test frequency on the frictional response, and to verify that the sharp peaks at 1 Hz is indeed introduced by the testing frequency itself, we conducted additional tests at 2 Hz using heat-treated Inconel and stainless steel 316 as a reference under the same testing condition (8 N load, 700 ºC, Al_2O_3 counter body). These results are summarized in Supplementary Figures 15-16. Indeed, for 2 Hz tests using either Inconel or stainless steel samples, the sharp peak shifts to 2 Hz, as indicated by the green dashed lines. With the 2 Hz wear test, it is also noticed that the phase transition feature in HT700 sample disappeared. In other words, the slope at frequencies below the test frequency is different for that above the test frequency at 1 Hz, but the same at 2 Hz. This could be due to less oxidation at higher sliding frequency, which results in less noticeable phase transition, hence resumes the traditional linear relationship in the power spectrum. Nonetheless, more work is required to systematically investigate the frequency-dependent instabilities due to stick-slip and phase transitions in the future.

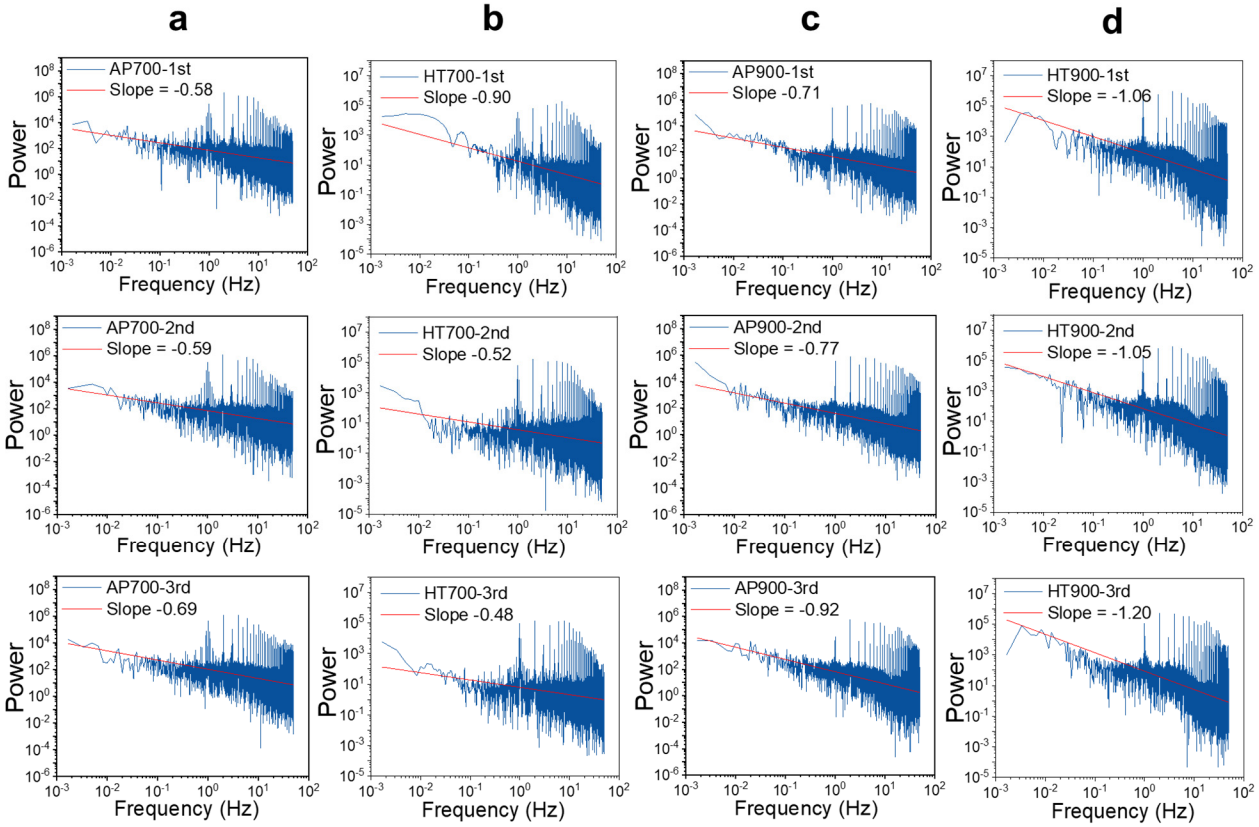

Supplementary Figure 14. Power spectra of raw COF data for a AP700, **b** HT700, **c** AP900, and **d** HT900 samples. 1st, 2nd, and 3rd represent three repeated tests.

3.5.Effects of testing frequency

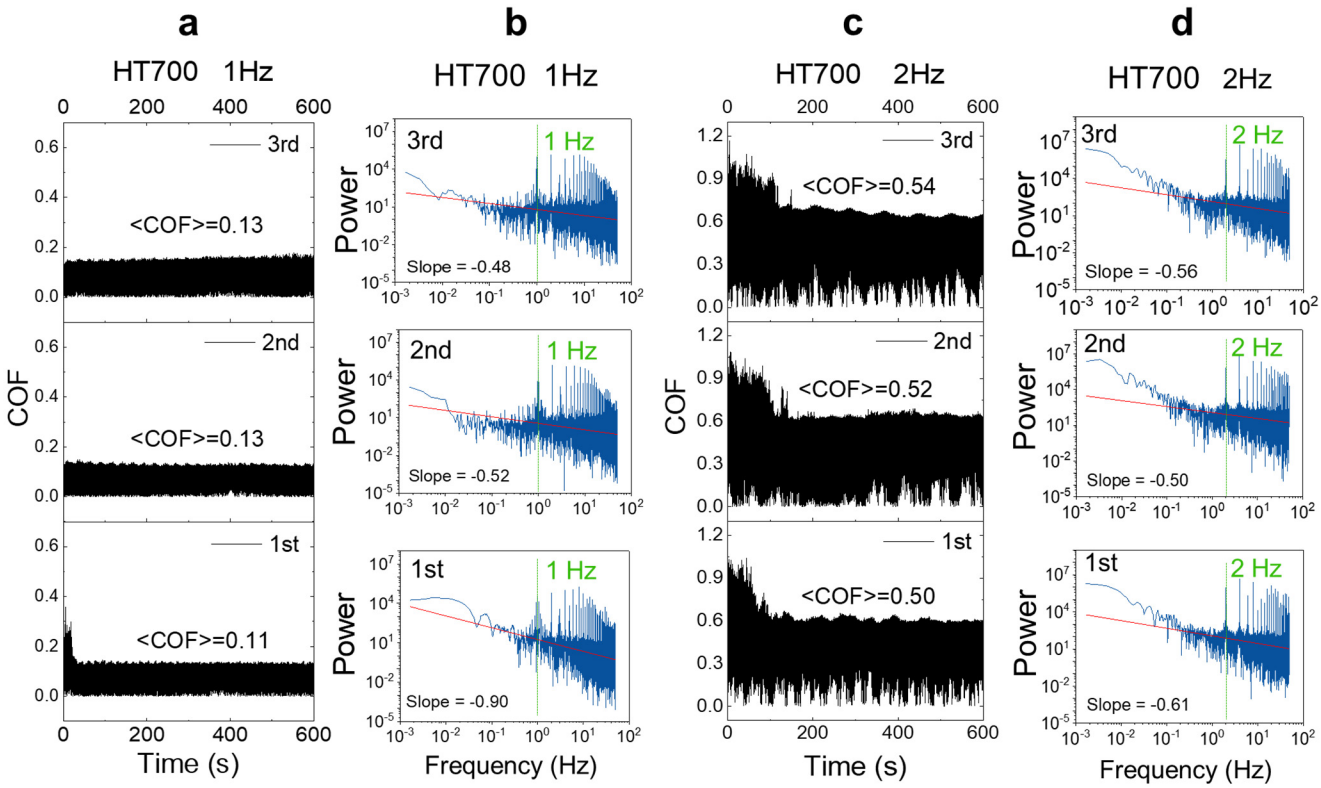

Supplementary Figure 15. Raw COF data as a function of testing frequency. a,c COF and **b,d** power spectrum of HT700 sample. 1st, 2nd, and 3rd represent three repeated tests.

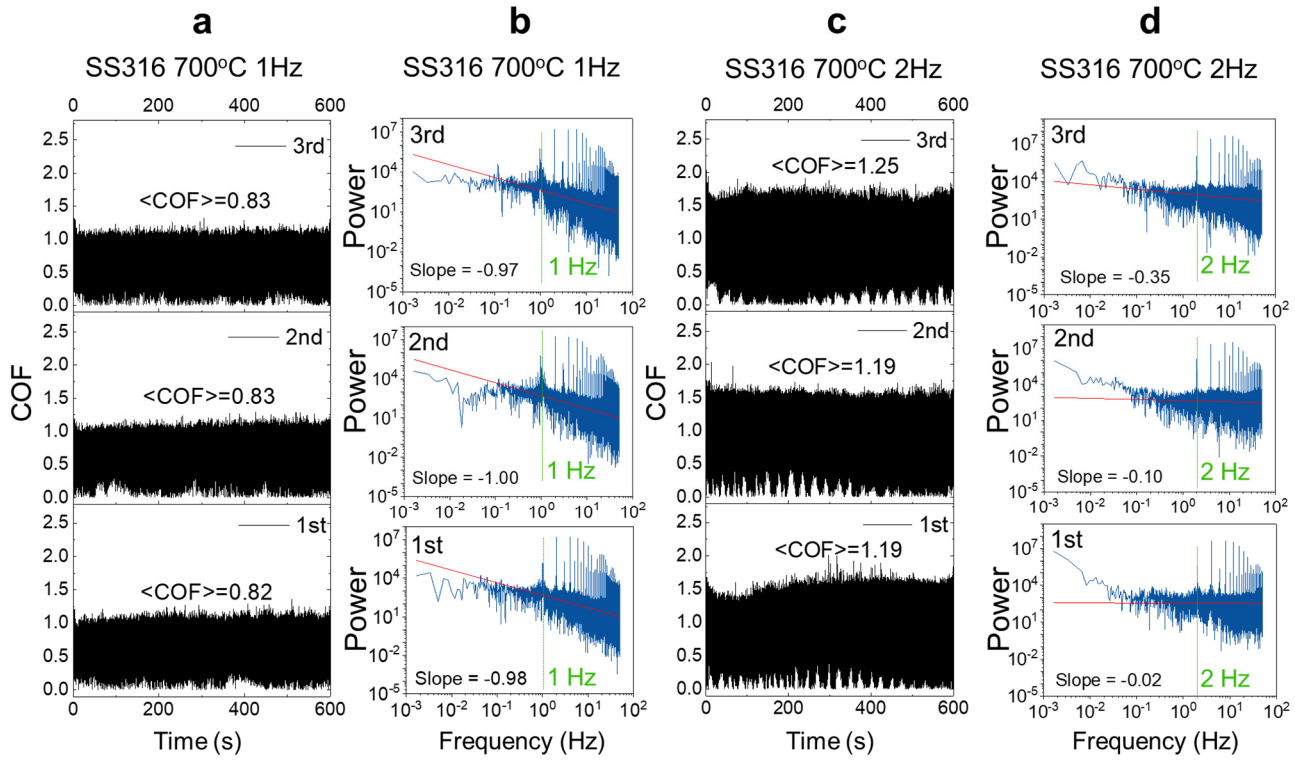

Supplementary Figure 16. Raw COF data as a function of testing frequency. a,c COF and **b,d** power spectrum of stainless steel 316 at 700 °C. 1st, 2nd, and 3rd represent three repeated tests.

4. Characterization of surface structure and chemistry

4.1.SEM and EDS results of Inconel samples

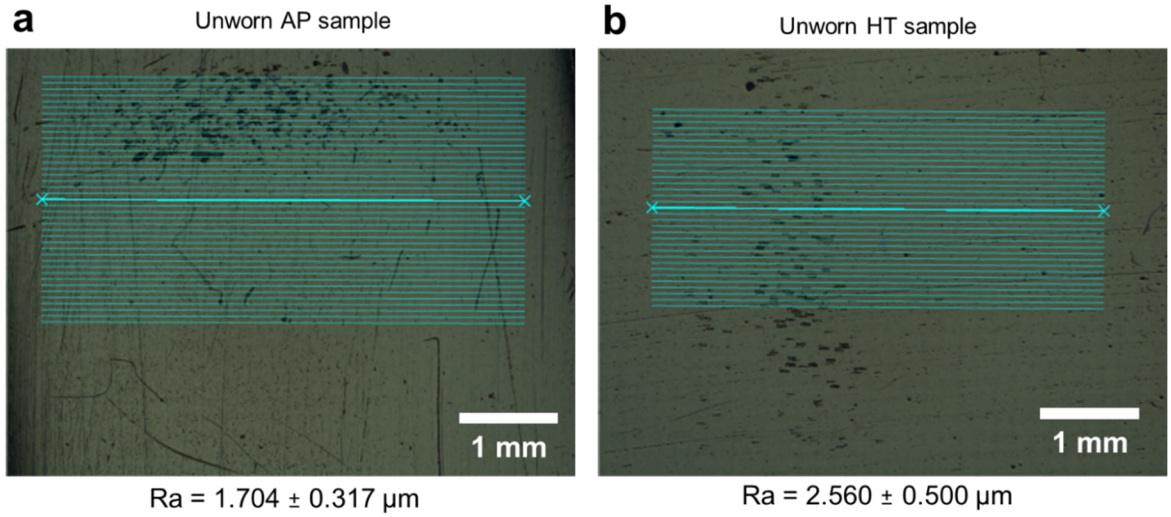

Supplementary Figure 17. Surface roughness from AP and HT samples before wear test. Optical images of unworn **a** AP and **b** HT Inconel 718 samples with scan regions overlayed for surface roughness measurement. The reported Ra values are calculated as the average of the surface's peaks and valleys.

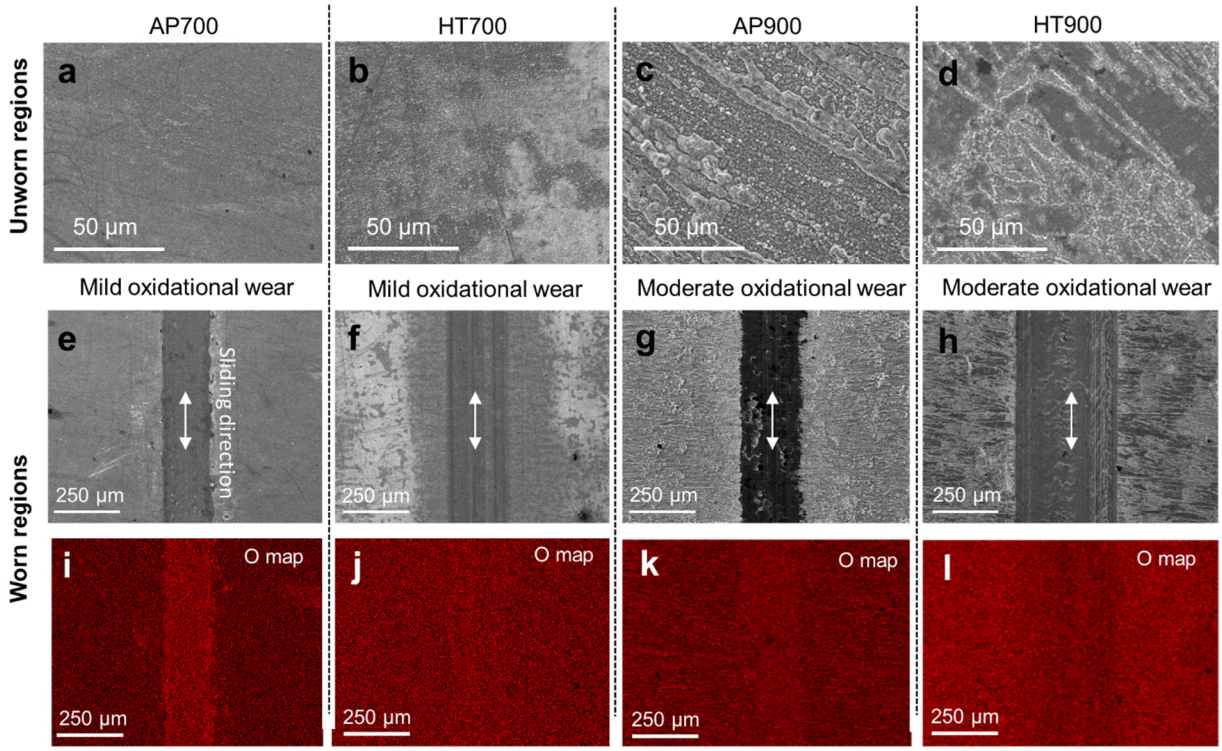

Supplementary Figure 18. Surface morphology from unworn and worn regions on Inconel 718 samples. SEM images of surfaces from **a-d** unworn and **e-h** regions, and **i-l** the corresponding oxygen elemental maps of AP700, HT700, AP900, and HT900 samples. Arrows in **e-h** represent the sliding direction.

Note on the wear mechanism in Figure 18:

As previously observed in the surface analysis of Al_2O_3, material transfer predominantly occurs from the oxidized Inconel surface to the ball, suggesting that the wear debris mainly originates from the oxide layer on Inconel. Supplementary Figure 18e-h shows a smooth wear track surface morphology in HT700 sample, consistent with its low COF, where the oxide acts as a lubricant layer, also known as a 'wear-protective layer' [49]. In the worn regions of HT700, grooves in the sliding direction are primarily due to substrate deformation under shear stress. Conversely, the wear region of AP700 shows higher oxygen content (Supplementary Figure 18i) compared to the unworn area, likely due to the agglomeration, compaction and/or sintering of oxidized wear debris on the track. This accumulated oxide layer has not reached the critical thickness for spallation, remaining largely intact on the wear surface. However, unlike HT700, this oxide accumulation does not reduce the wear rate due to the abrasive nature of the oxide formed. Despite this, the wear rates of AP700 and HT700 remain within the same order of magnitude (~10^{-6} $mm^3/(N*m)$), classifying them as mild oxidative wear. For AP900 and HT900, the wear track regions have similar oxygen concentrations as the unworn areas (Supplementary Figure 18k-l), indicating a balance between wear debris compaction and removal. At these higher temperatures, both oxidation and material removal rates are increased compared to those at 700 °C, leading to their classification as moderate oxidative wear.

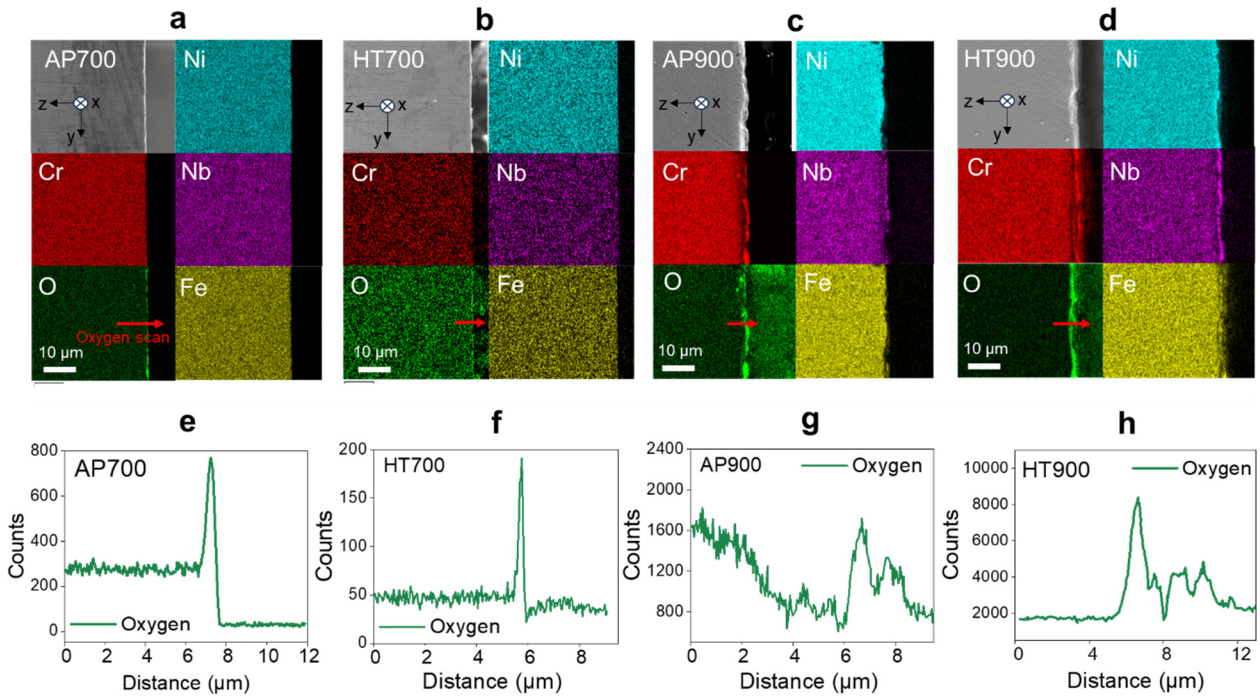

Supplementary Figure 19. Characterization of worn surface oxide layer of Inconel 718 samples. SEM image and corresponding elemental maps of **a** AP700, **b** HT700, **c** AP900, and **d** HT900 cross-sectional sample**s. e-h** The corresponding oxygen elemental maps from the arrow directions in **a-d**. x- and z- in the inset of **a-d** indicate the sliding and normal direction respectively, as defined in Supplementary Figure 8a.

4.2.GIXRD results of Inconel samples

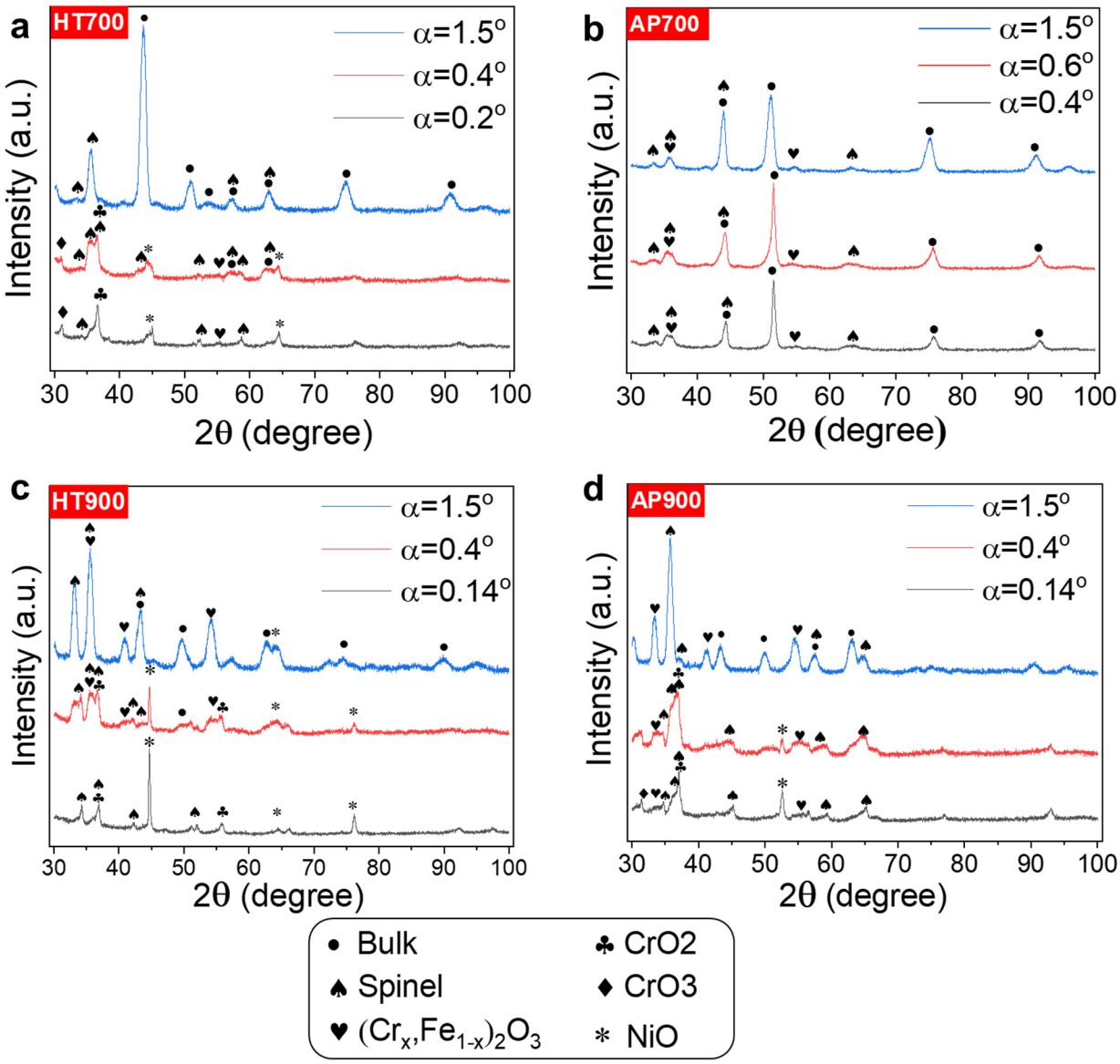

Supplementary Figure 20. Phase identification of the worn surface oxide on Inconel 718 samples. GI-XRD results for **a** HT700, **b** AP700, **c** HT900, and **d** AP900 sample within the wear track region, where each phase is labeled using the index legend at the bottom. The incident angle (α) is varied to probe the ultrathin surface oxide layer where the smallest α value indicates the outermost surface.

4.3.XPS results of Inconel samples

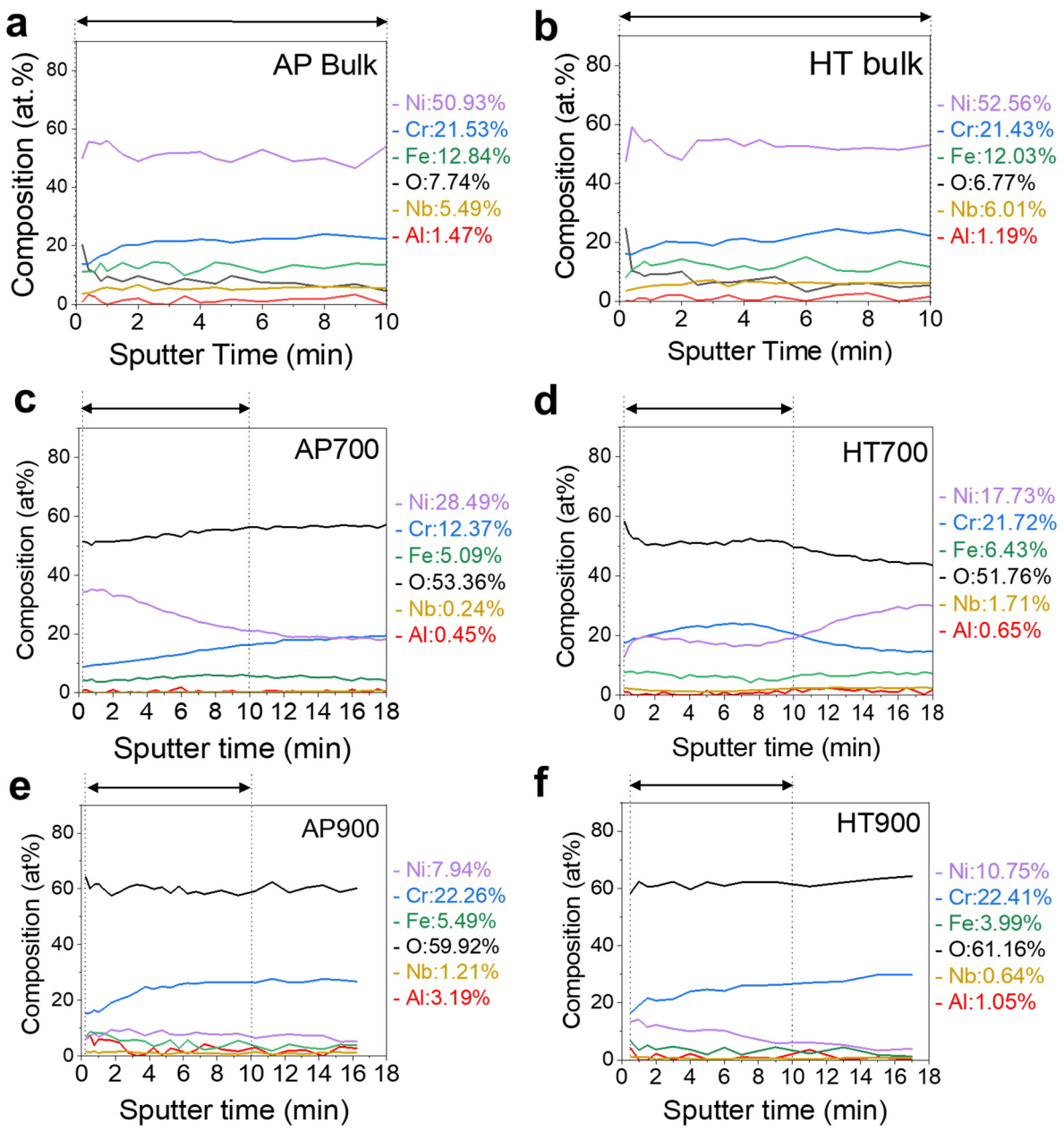

Supplementary Figure 21. XPS depth profile of Inconel 718 samples. XPS line profiles of O, Al, Cr, Fe, Ni, and Nb from the (a, b) unworn bulk samples, and (c-f) wear track region of AP700, HT700, AP900, and HT900 samples. Sputter time 0 corresponds to the outermost surface and higher sputter time corresponds to deeper location below the surface. The compositions listed on the right shows the average compositions (at.%) from the first 10 min of sputter time of each sample.

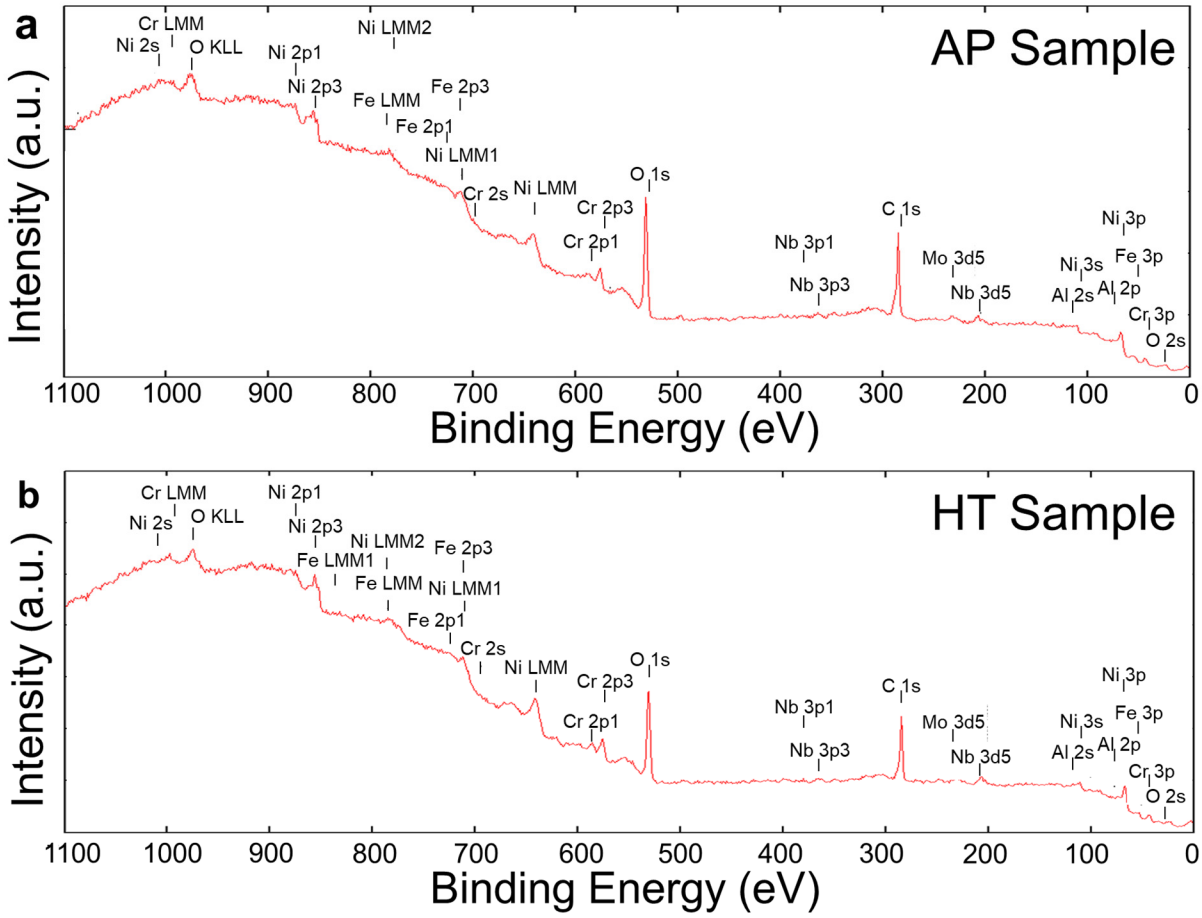

Supplementary Figure 22. XPS survey profile of Inconel 718 samples **a** AP sample and **b** HT sample before wear tests.

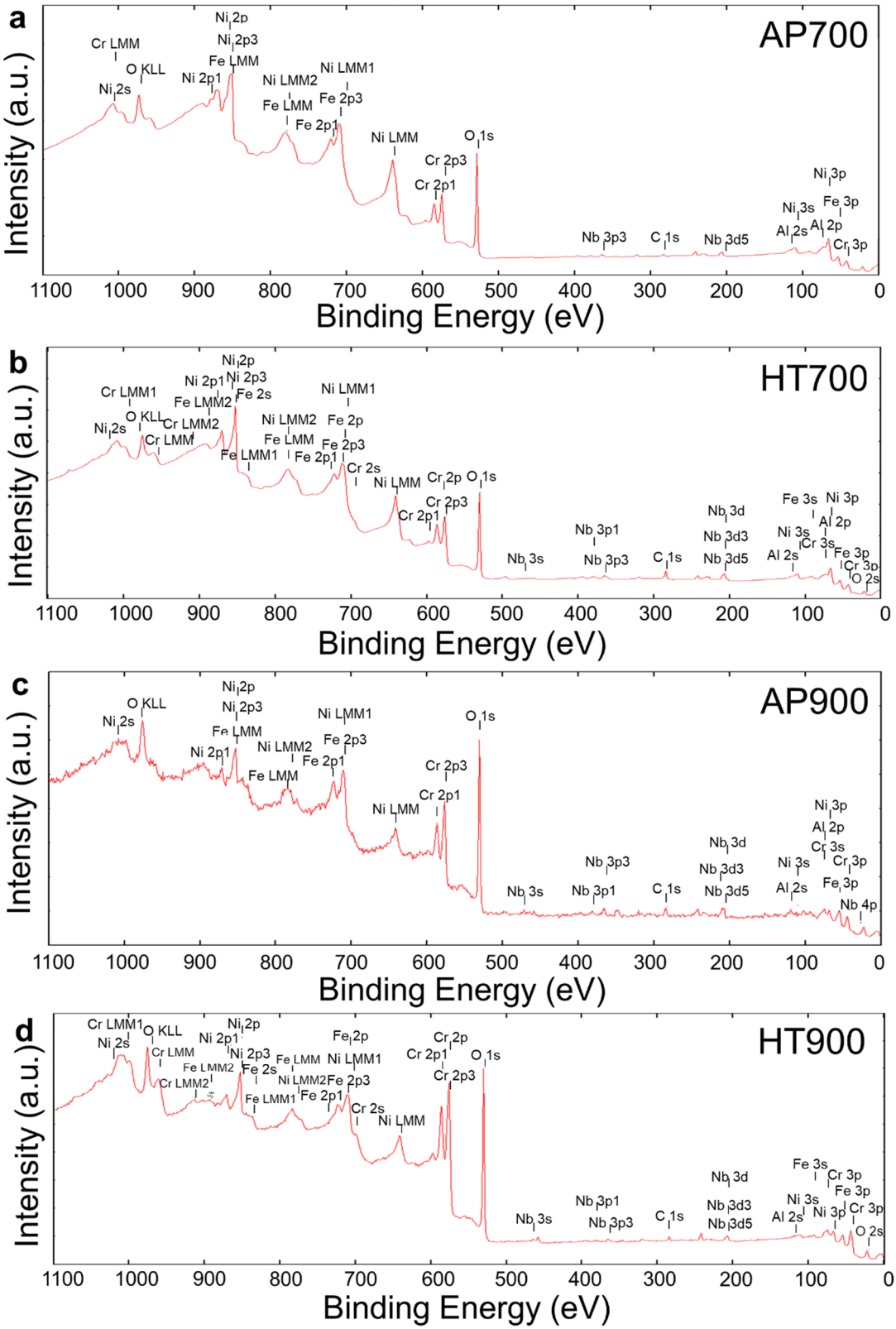

Supplementary Figure 23. XPS survey profile of Inconel 718 samples. **a** AP700**, b** HT700, **c** AP900, and **d** HT900.

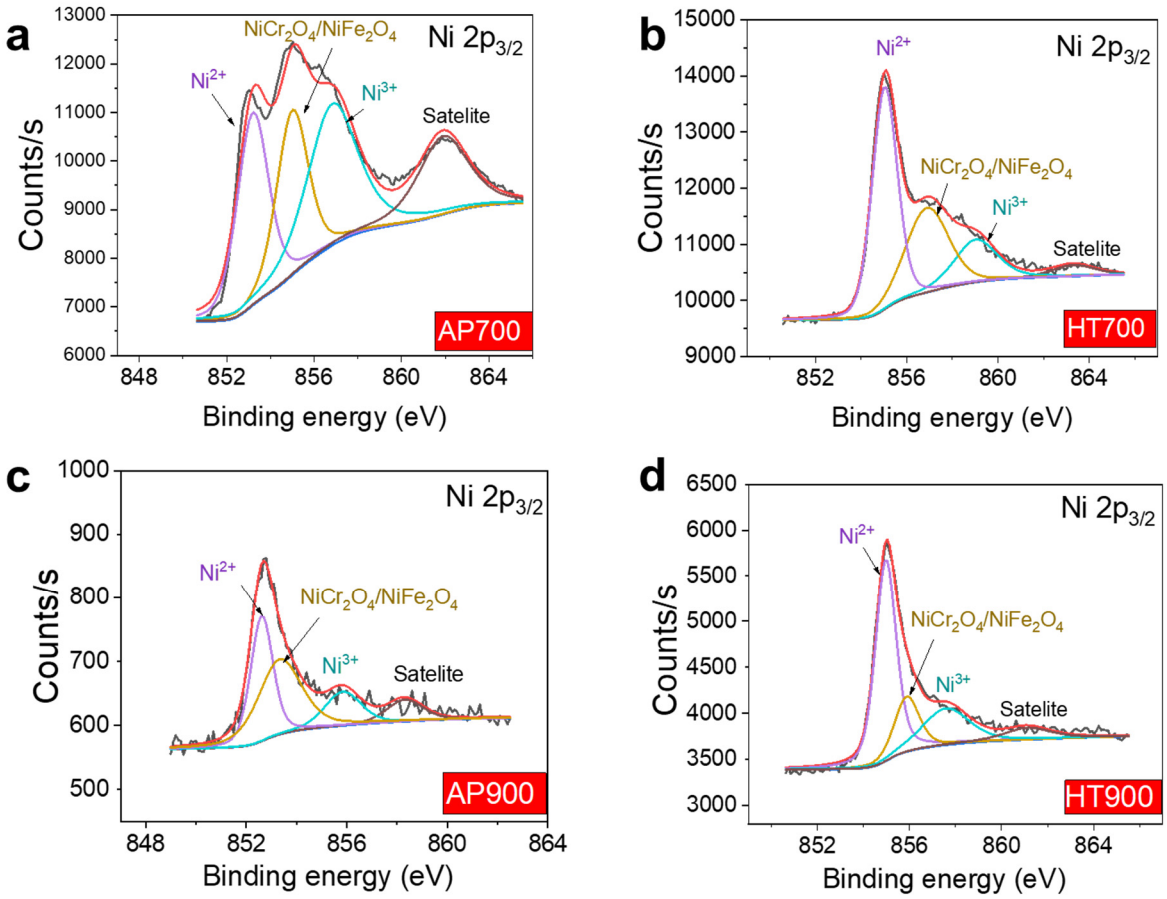

Supplementary Figure 24. Surface oxide oxidation state analysis. High-resolution XPS spectra of Ni 2p from the wear track regions of **a** AP700, **b** HT700, **c** AP900, and **d** HT900 sample.

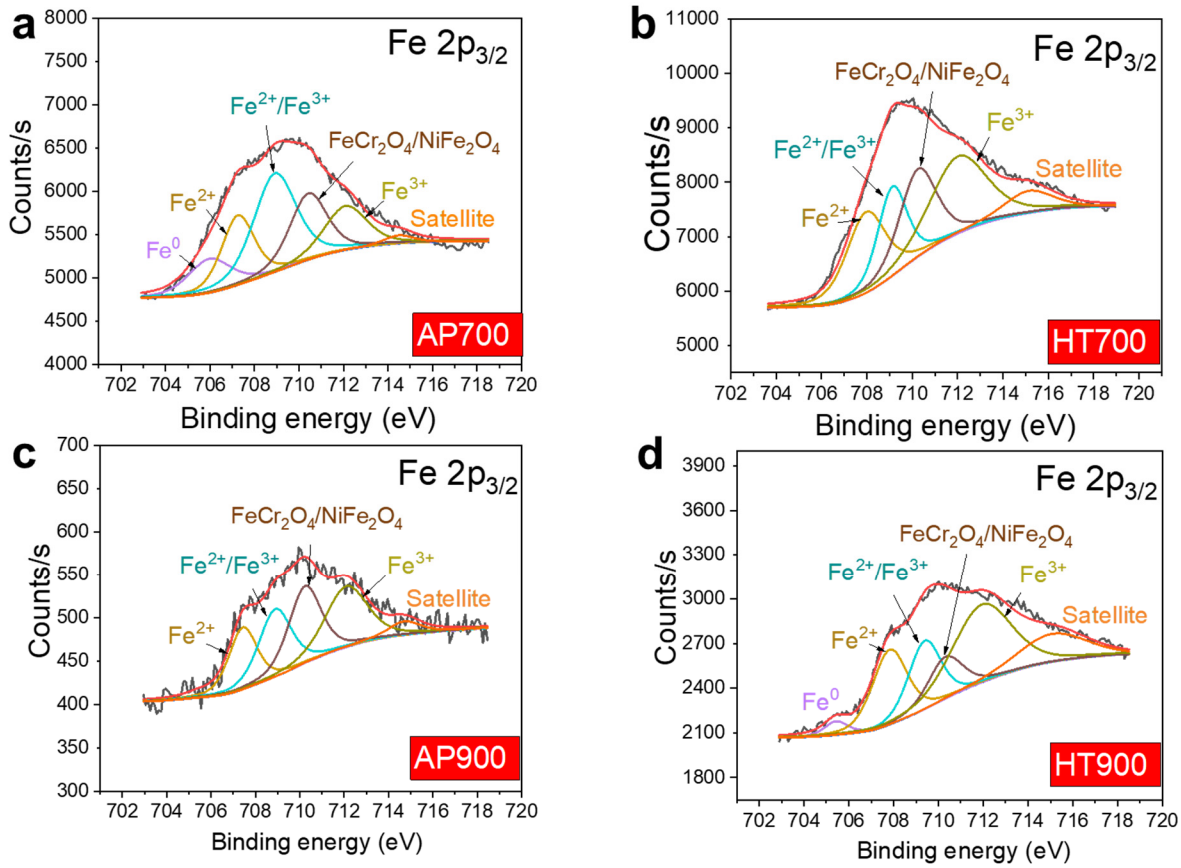

Supplementary Figure 25. Surface oxide oxidation state analysis. High-resolution XPS spectra of Fe 2p from the wear track regions of **a** AP700, **b** HT700, **c** AP900, and **d** HT900 sample.

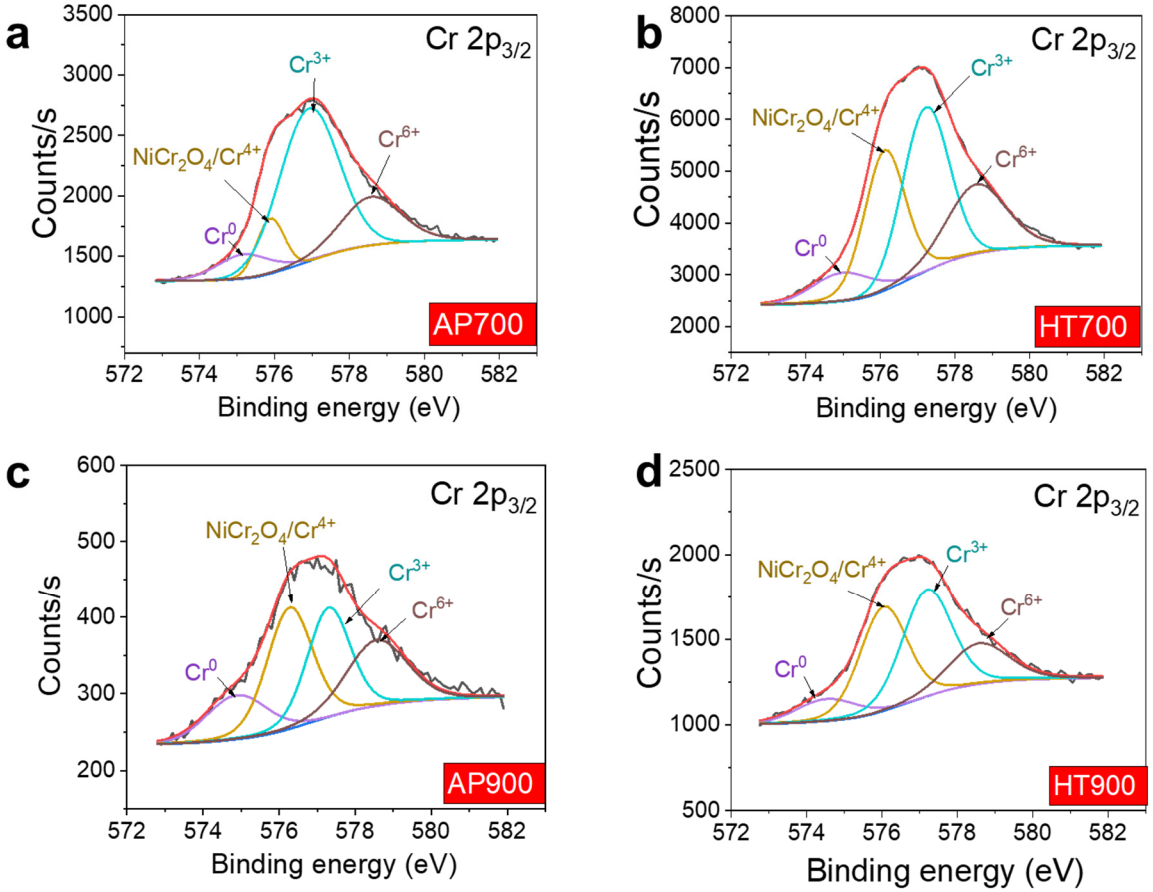

Supplementary Figure 26. Surface oxide oxidation state analysis. High-resolution XPS spectra of Cr 2p from wear track regions of **a** AP700, **b** HT700, **c** AP900, and **d** HT900 sample.

4.4.TEM results of Inconel samples

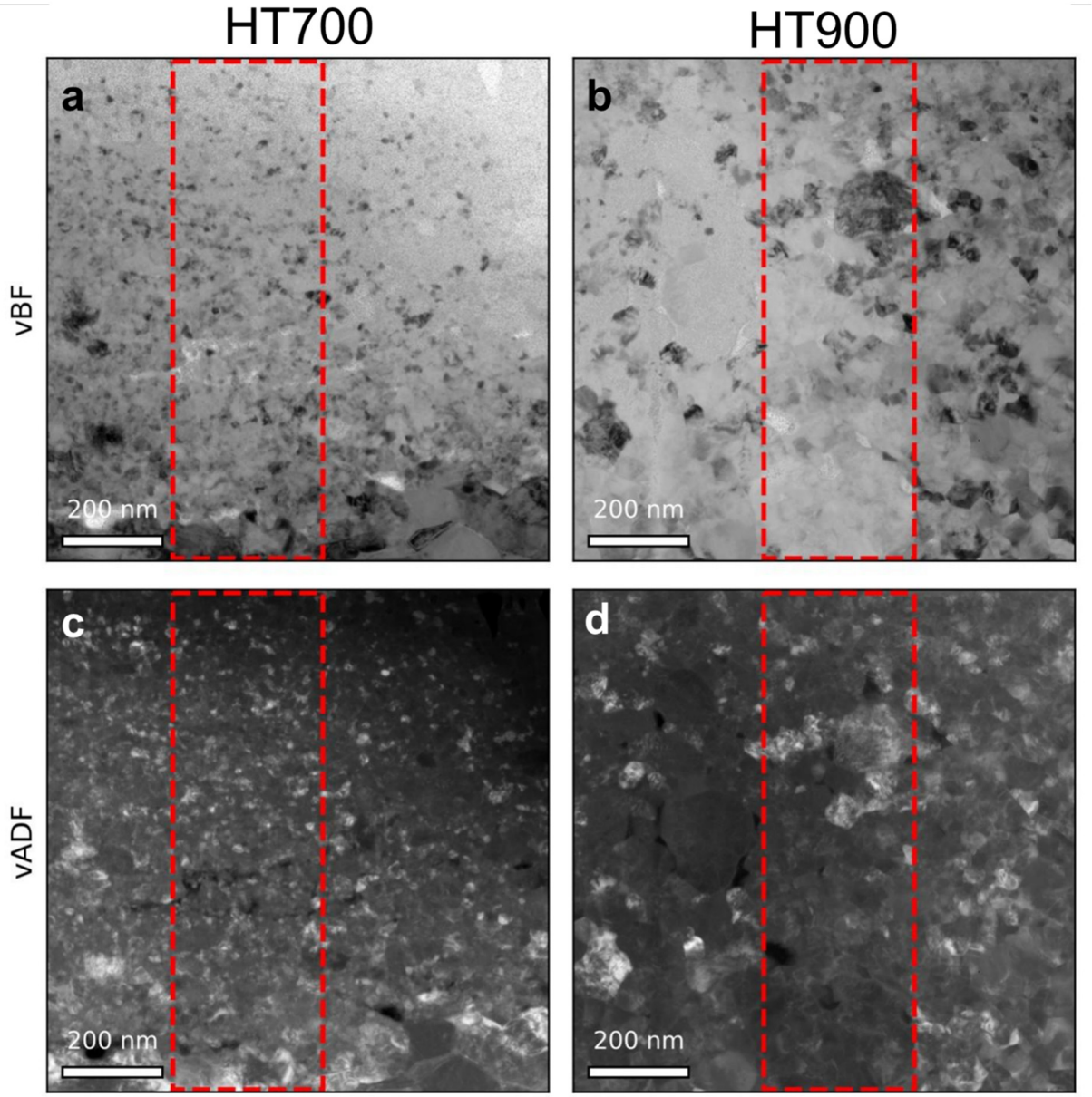

Supplementary Figure 27. Virtual bright field and annular dark field reconstructed STEM images of the oxide regions of the HT700 and HT900 cross-sectional samples highlighting the difference in apparent grain size between the samples. The regions associated with the phase maps in Fig. 4(c, d) are indicated with red dashed boxes.

To provide additional insight into the typical grain sizes of the HT700 and HT900 samples, we created virtual bright field and annular dark field reconstructions from the 4D-STEM data collected

in the oxide regions of the two samples. An integration range of 0-3 mrad was used to construct the virtual bright field images and 15-38 mrad was used to construct the virtual annular dark field images. We find that the feature sizes in the phase maps in Fig. 4(c, d) are consistent with the grain sizes observed with these virtual images. From the 1 x 1 μm^2 virtual images, we identify the grain size in the HT700 sample to be on the order of 5-30 nm and in the HT900 sample to be on the order of 50-200 nm.

4.5.SEM and EDS results of Al_2O_3 ball

The surface roughness of Al_2O_3 is primarily influenced by its porosity. The initial surface morphology of Al_2O_3 was characterized using SEM, as shown in Supplementary Figure 28 a-b. The porosity on the Al2O3 surface measures to be 3.84 ± 1.84 μm. When compared to the surface morphology of the ball after the wear test against Inconel samples (Supplementary Figure 28 c-f), it is observed that these defects within the wear contact areas are largely covered by the transfer layer. As a result, they become less significant in determining the nature of the two-body contact after the initial running-in period.

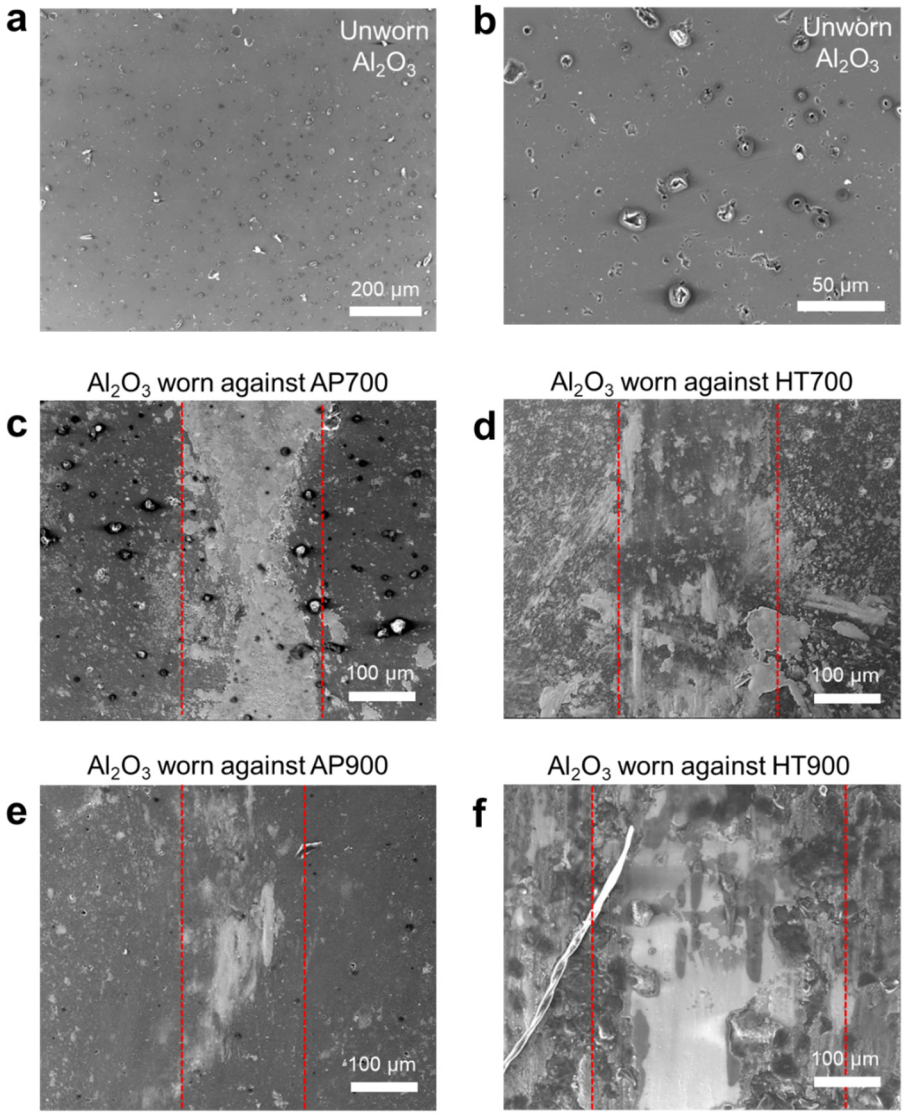

Supplementary Figure 28. Surface morphology from as-received and worn Al_2O_3 surface. SEM images of surfaces from **a-b** as-received, unworn surface of Al_2O_3 ball, and **c-f** contact area on Al_2O_3 ball after wear tests against **c** AP700, **d** HT700, **e** AP900, and **f** HT900 sample. Dashed lines in **c-f** represent the boundary of contract area.

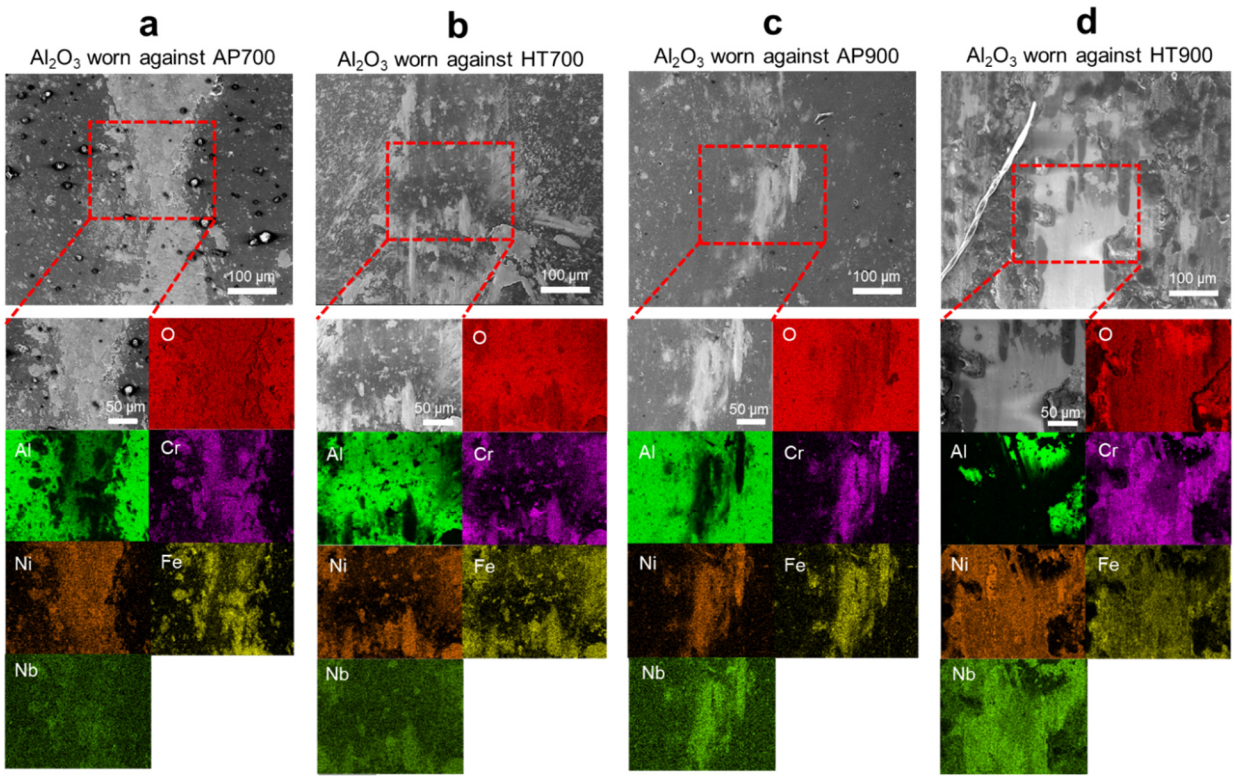

Supplementary Figure 29. Surface morphology and elemental mappings from worn Al_2O_3 surface. SEM images and corresponding EDS mappings of Al_2O_3 ball after wear test against **a** AP700, **b** HT700, **c** AP900, and **d** HT900 sample.

a Al_2O_3 worn against AP700

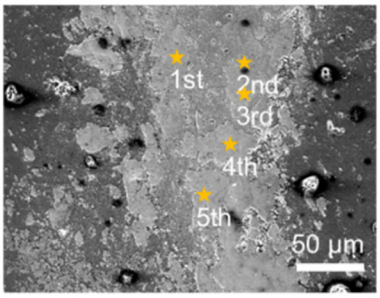

	Cr	Fe	Ni	Nb	Al	O
1st	8.6	9.8	10.7	N/A	8.2	46.0
2nd	7.6	12.0	8.1	N/A	9.6	45.0
3rd	9.6	16.4	5.7	0.3	6.3	46.5
4th	5.1	11.0	7.0	0.4	8.4	46.3
5th	7.2	16.0	7.1	0.3	6.6	46.3
Avg. (at.%)	**7.6**	**13.0**	**7.7**	**0.3**	**7.8**	**46.0**
SD (at.%)	1.51	2.68	1.67	0.05	1.22	0.53

b Al_2O_3 worn against HT700

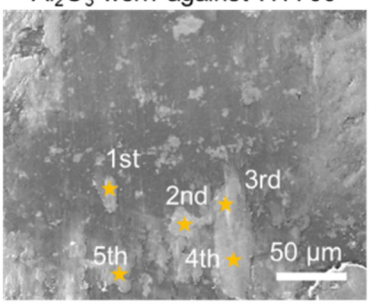

	Cr	Fe	Ni	Nb	Al	O
1st	4.3	3.3	10.7	0.8	8.3	38.7
2nd	11.6	8.1	9.4	1.8	1.7	44.5
3rd	7.1	6.5	11.9	1.1	2.6	45.4
4th	7.3	6.7	14	1.3	1.9	43.4
5th	5.7	6.2	12.9	0.8	7.7	44.4
Avg. (at.%)	**7.2**	**6.2**	**11.8**	**1.2**	**4.4**	**43.3**
SD (at.%)	2.45	1.57	1.61	0.37	2.93	2.38

c Al_2O_3 worn against AP900

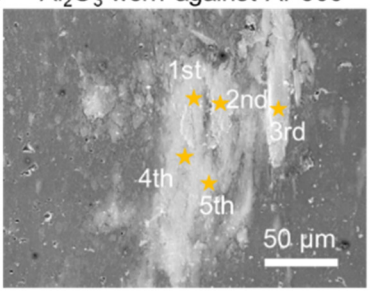

	Cr	Fe	Ni	Nb	Al	O
1st	8.2	7.2	8	1.6	6.1	45.6
2nd	10.4	6.1	7.4	2	6.3	47.4
3rd	11.1	7.4	11.3	1.4	2	46.2
4th	5.8	5.3	7.8	1.1	13.5	45.2
5th	8	9	10.9	1.1	5	46.6
Avg. (at.%)	**8.7**	**7.0**	**9.1**	**1.4**	**6.6**	**46.2**
SD (at.%)	1.89	1.26	1.67	0.34	3.79	0.77

d Al_2O_3 worn against HT900

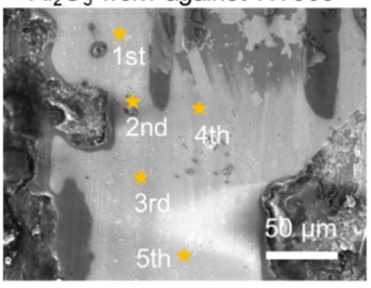

	Cr	Fe	Ni	Nb	Al	O
1st	3.6	7.4	10.3	0.7	0.4	30.8
2nd	1.5	0.4	1.7	0.2	21	33.3
3rd	7.8	7.6	4.7	1.2	2.9	32.6
4th	4.8	5.2	9.4	0.8	5.4	36.2
5th	9.5	5	7.7	1.5	2.1	34.9
Avg. (at.%)	**5.44**	**5.12**	**6.76**	**0.88**	**6.36**	**33.6**
SD (at.%)	2.88	2.59	3.17	0.44	7.5	1.864

Supplementary Figure 30. EDS composition analysis from worn Al_2O_3 surface. SEM images (left) and compositions (right) in atomic percent (at.%) of Al_2O_3 ball after wear test against **a** AP700, **b** HT700, **c** AP900, and **d** HT900 sample. Stars in SEM images (left) mark the EDS point analysis locations listed in the table (right). Avg. and SD in the table represent average and standard deviation from all measurements respectively.

4.6. Discussion on material transfer

In Supplementary Figure 28, the surface morphology of the Al_2O_3 counterbody before (Supplementary Figure 28a-b) and after (Supplementary Figure 28c-f) high-temperature wear tests against AP700, HT700, AP900, and HT900 Inconel samples was characterized using SEM. The dashed lines in Supplementary Figure 28c-f indicate the boundary of the contact area. Notably, in the Al_2O_3 sample worn against the HT900, a long fiber is present near the boundary of the wear region, likely due to accidental surface contamination from tissue paper during sample handling. Since the Al_2O_3 ball was already coated with a thin layer of gold for conductivity before SEM imaging, several attempts were made to remove this fiber using compressed air, but unfortunately, these efforts were unsuccessful. Consequently, EDS mapping was performed in an adjacent region to avoid this contamination (see Supplementary Figure 29d below).

In terms of surface morphology, after the wear test at 700 °C, the Al_2O_3 ball used against HT700 (Supplementary Figure 28d) exhibits discontinuous patches of light-colored regions within the contact area. In contrast, the ball used against AP700 shows a relatively uniform light-colored region across the entire contact area. Additional EDS mappings of these two surfaces (Supplementary Figure 29a-b) reveal that these light-colored regions have lower concentrations of Al and higher concentrations of Ni, Cr, Fe, and Nb compared to the unworn regions, which contain only Al and O.

Quantitative compositional analysis from EDS point analysis at five random locations within these light-colored areas (Supplementary Figure 30) indicates concentrations of approximately 5.4-8.7 at.% Cr, 5.1-13 at.% Fe, 6.8-11.8 at.% Ni, 0.3-1.4 at.% Nb, 4.4-7.8 at.% Al, and 33.6-46.2 at.% O. This suggests that these materials were primarily transferred from the Inconel sample surface to the Al_2O_3 ball during the high-temperature wear test. The surface morphologies and material transfer on the ball also correlate well with the wear track depth profiles on the Inconel surfaces (Supplementary Figures 32b-c), where the HT700 sample shows shallow and flat wear profiles, and the AP700 sample displays deeper and curved profiles. At 900 °C, the Al_2O_3 ball tested against HT900 shows a wider wear track compared to that tested against the AP900 sample (Supplementary Figures 28e-f). Notably, the ball used against AP900 has the smallest contact width among all samples, which is consistent with the wear depth profiles observed on the Inconel samples (Supplementary Figures 32b-c).

To confirm that material transfer primarily occurs from the Inconel sample to the Al_2O_3 ball, additional XPS depth analysis, including the Al element, was performed on the unworn and worn surfaces of the Inconel samples, as shown earlier in Supplementary Figure 21. Note that as shown in Supplementary Figure 21a-b, in the unworn bulk Inconel samples, XPS analysis of the top surface (averaging the composition from sputter time 0 to 10 min) shows AP and HT samples already have an Al concentration of 1.47 at.% and 1.19 at.% respectively. After wear tests at 700 °C, these is not much Al concentrated on the Inconel sample surface, as evidenced by the lower Al content (0.45-0.65 at.%) in the surface oxide layer, as compared to the slightly higher Al content (1.05-3.49 at.%) observed at 900 °C. This finding is consistent with the TEM cross-section analysis (see Figure 4b in the paper) where there are some Al clusters ~ 200 nm within the surface oxide

of HT900 sample. Such very small amount of Al detected on the surfaces of the AP900 and HT900 samples indicate either there is some material transfer from the ball to the Inconel surface or enhanced diffusion of Al from the Inconel bulk to the surface. At this point, we are not able to rule out either of the two possibilities. Nonethless, based on these characteristics, we conclude that in the Inconel/Al_2O_3 contact pair, material transfer primarily occurs from the Inconel surface to the Al_2O_3 ball.

It is worth noting that at 700 °C, the HT700 sample has a higher hardness than the AP700 sample (see high temperature hardness data in the Response to Reviewer 1 Q1.6 and Supplementary Figure 5), which would result in a smaller contact area per Archard's law [50]. However, the opposite is observed in this case. Both the ball and the Inconel sample show a relatively large contact area, characterized by discontinuous rather than continuous material transfer between the two surfaces. This suggests that the oxide layer formed on HT700 is lubricious, and its formation on the discrete contact areas leads to a relatively large yet flat worn surface on the Inconel, contributing to the low wear rate of HT700. During dry sliding wear, the initial contact area is often small during the running-in period, which typically develops into more severe wear over time, resulting in deep and curved surface profiles, such as those observed on AP700 (Supplementary Figure 32b). The fact that the contact area remains patchy on the Al_2O_3 ball used against HT700 (Supplementary Figure 32b) further confirms the lubricity of the oxides formed at the contact points, which helps lubricate the sample surface and prevents it from progressing into more severe wear.

5. Nanomechanical measurements

5.1. Nanomechanical measurement procedure

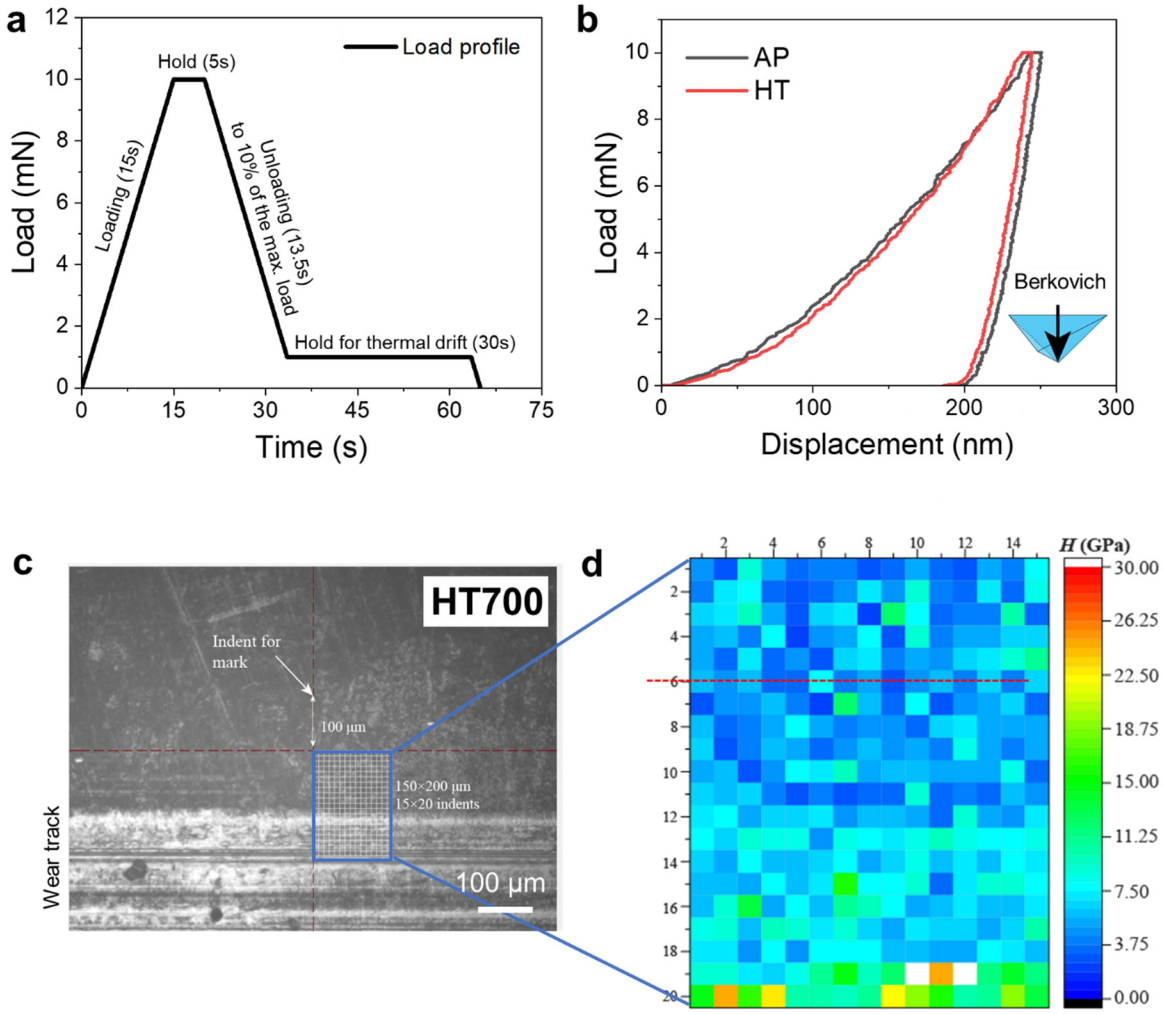

Supplementary Figure 31. Nanoindentation setup and results for SLM Inconel 718 samples. **a** Load profile for each indent with a maximum load of 10 mN, where the extended loading and unloading time ensured smooth curves for precise interpretation. **b** Typical indentation results for the AP and HT samples. Inset in **b** show a schematic of the Berkovich diamond tip. **c** Nano-indentation setup and **d** hardness map of HT700 sample.

5.2.Nanomechanical properties of worn surfaces

Supplementary Table 3. Nano-indentation hardness (H), reduced elastic modulus (E_r), E_r/H, and Vickers hardness (HV) measured from the unworn surface of AP and HT samples, and wear track region of HT700, HT900, AP700, and AP900 samples.

Sample / Property	AP	HT	AP700	HT700	AP900	HT900
H (GPa)	5.57 ± 0.61	6.83 ± 0.76	8.69 ± 1.88	7.46 ± 5.35	15.96 ± 4.86	15.12 ± 5.36
E_r (GPa)	253.63 ± 16.77	283.69 ± 16.59	251.41 ± 19.34	232.99 ± 43.29	260.87 ± 36.24	260.54 ± 36.24
E_r/H	45.54	41.54	28.93	31.23	16.34	17.23
HV	360.9 ± 11.2	483.4 ± 13.4	397.6 ± 11.3	465.9 ± 18.6	449.0 ± 18.3	396.6 ± 18.1

The nanomechanical properties of worn surfaces, including hardness (H), reduced elastic modulus (E_r), and E_r/H were examined by nano-indentation, as summarized in Supplementary Figure 32d-h and Supplementary Table. 3. Typical load-displacement curves of both samples are shown in Supplementary Figure 31b. For the unworn samples, the HT sample had larger H (Figure 32d) and E_r, but lower E/H ratio than the AP sample (Figure 32d). The hardness increased from 5.57 GPa to 6.83 GPa (~ 22.6% increment) after heat treatment, likely due to the formation of various strengthening phases, as discussed previously. A lower E/H ratio also indicates that the HT sample is more wear-resistant than the AP sample [51, 52], which is largely consistent with the tribological results. For the worn samples tested at 700 ºC, the worn area hardness of both HT700 (7.46 GPa) and AP700 (8.69 GPa) are higher than that of the unworn samples (6.83 GPa for HT and 5.57 GPa for AP sample). A combination of wear-induced plastic deformation and the high temperature wear condition likely leads to further strengthening of the material. At 900 ºC, the worn surface shows much higher hardness (~ 15 GPa) accompanied by a large standard deviation of ~ 5 GPa. Such a large variation of surface hardness is likely due to the formation of surface oxide that covers the worn surface, which is indeed confirmed by cross-sectional elemental mapping shown in the Figure 3 of the main text. At 900 ºC, oxidation is more significant than 700 ºC, which leads to the formation of 2-4 μm thick oxides on both HT900 and AP900 samples. As shown in the nanomechanical maps in Supplementary Figure 32g,h, much higher hardness has been observed in the worn regions at 900 ºC than 700 ºC for both samples, likely due to thicker coverage of the surface oxides. Note that the maximum load of nanoindentation is 10 mN, which results in penetration depth of less than ~ 400 nm for the samples tested. Thus, nanoindentations made right on the oxides likely have higher hardness values than those indented on thin oxides or uncovered bare metal.

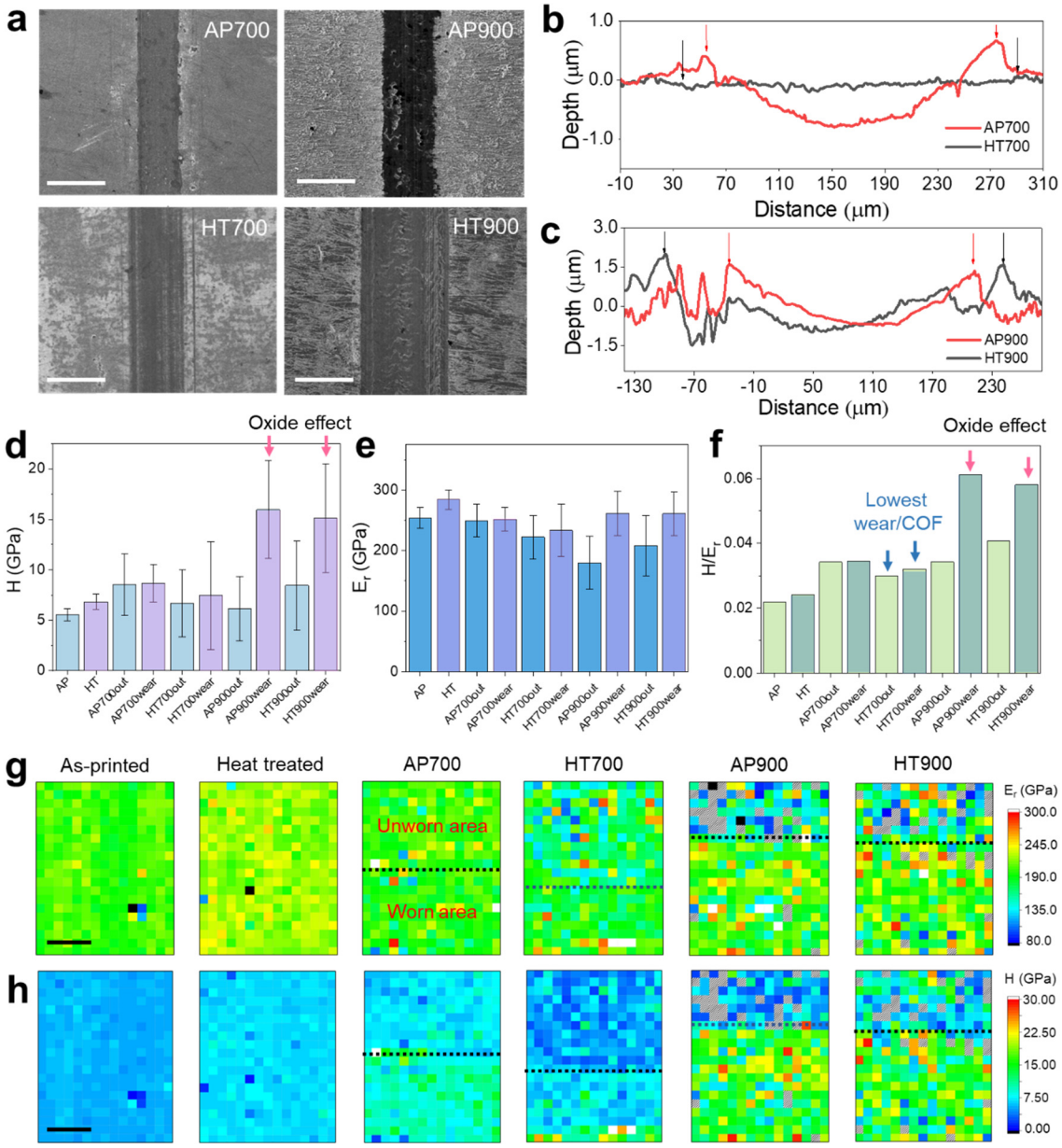

Supplementary Figure 32. Worn surface morphology and nanomechanical properties. a SEM images **b,c** surface profiles measured perpendicular to the sliding direction of worn surfaces of AP700, HT700, AP900, and HT900. Scale bar in **a**: 250 μm. Arrows in **b, c** indicate the edge of wear track. Summary of **d** hardness (H), **e** reduced elastic modulus (E_r), **f** E_r/H ratio, and maps of **g** E_r and **h** H from the worn surfaces of HT and AP samples after high temperature wear test at 700 °C and 900 °C. Dashed lines in **g, h** separates the unworn (top area) and worn regions (bottom area). Scale bar: 5 μm. All figures in **g** and **h** have the same scale bar.

6. Mechanical stability and property of oxides

6.1. Reported hardness of oxides

Supplementary Table 4. Data for hardness and oxide crystal structure from Ref [53].

Oxide Type	Crystal Structure	Hardness (kg/mm^2)
Fe_3O_4	spinel structure	690
Co_3O_4	spinel structure	713
α-Fe_2O_3	corundum structure	986-1219
Cr_2O_3	corundum structure	1820-3270
α-Al_2O_3	corundum structure	2160

As shown in Supplementary Table 4, oxides with a corundum structure have hardness in the range of 986-3270 kg/mm², while those with a spinel structure range from 425 to 713 kg/mm². Spinel-structured oxides generally exhibit lower hardness compared to corundum-structured oxides. This trend is also observed in shear modulus, which is similarly related to bond strength. For example, $NiCr_2O_4$ has a lower shear modulus than Cr_2O_3, consistent with their hardness differences. Nano-indentation tests on the wear tracks reveal hardness values of 7.46 GPa for HT700, 8.69 GPa for AP700, 15.12 GPa for HT900, and 15.96 GPa for AP900, with HT700 showing the lowest hardness. Given that the indentation depths are under ~400 nm, these results likely reflect the mechanical response of the oxide layers.

6.2.Thermodynamic calculations

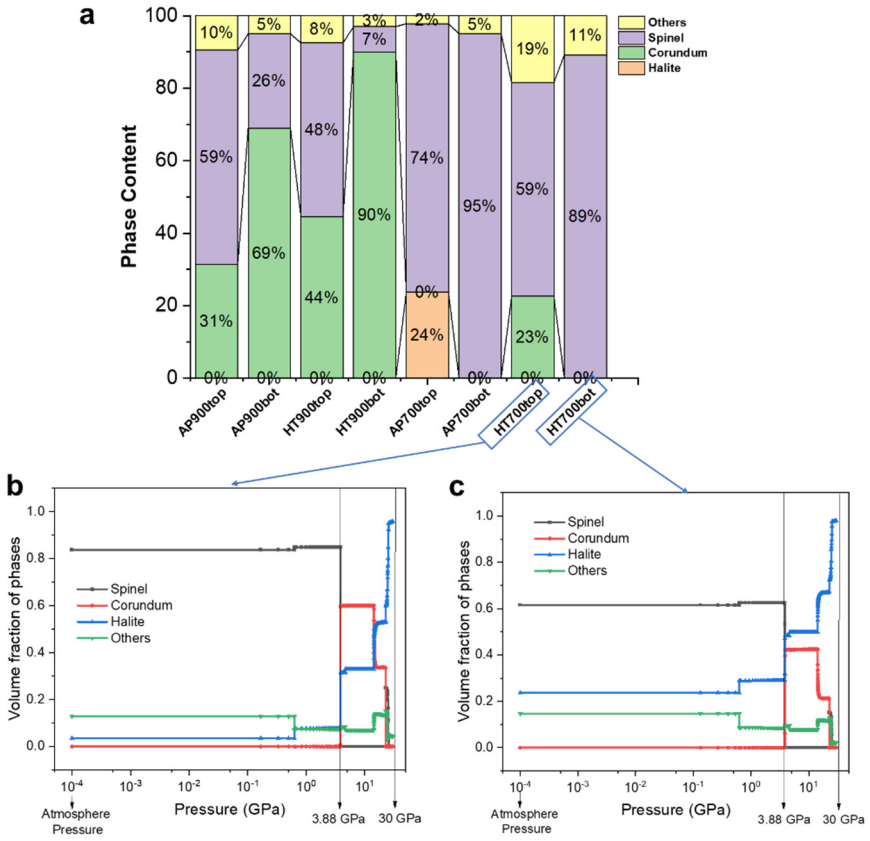

Supplementary Figure 33. Calculated oxide phase fraction on the worn surface. Simulated phase fraction (a) at the worn surface, and (b-c) under hydrostatic compressive pressure of all samples using Thermo-calc software TCOX12 database, version 2023b, where 'top' and 'bot' after each sample name represents the outmost and inner oxide respectively. Composition data is from XPS depth profile.

6.3.DFT calculations

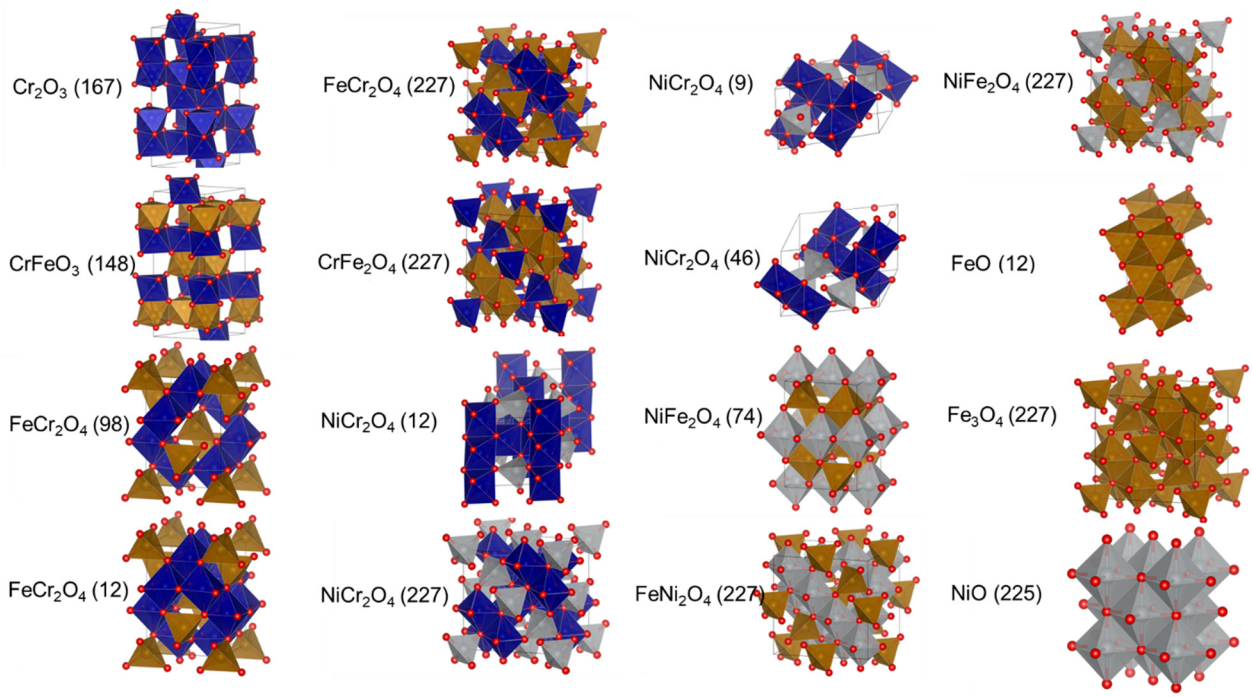

Supplementary Figure 34. Metal oxide structures used in DFT calculations. Structures for all metal oxides calculated in the **Supplementary Table 5**. The numbers in the parentheses represent the space group number of the corresponding structure.

Supplementary Table 5. Summary of the shear modulus, cohesive energy, and formation energy of various oxides from DFT calculations in this study. In the first column, the composition of the oxide is followed by its space group international number and crystal system in the parentheses. For the unstable oxide, shear modulus listed are obtained from literature experimental or computational results.

Oxide	Shear Modulus (GPa)	Mechanical Stability under minor shear	Cohesive Energy (eV/atom)	Formation Energy (eV/atom)
Cr_2O_3 (167, trigonal)	126.4	Stable	-5.61	-2.133
$CrFeO_3$ (148, trigonal)	103.9	Stable	-5.593	-1.911
$FeCr_2O_4$ (98, tetragonal)	77.7	Stable	-5.735	-2.076
$FeCr_2O_4$ (12, monoclinic)	69.7	Stable	-5.735	-2.077
$FeCr_2O_4$ (227, cubic)	30.9 [54]	Not stable	-5.598	-1.939
$CrFe_2O_4$ (227, cubic)	48.9 [55]	Not stable	-5.320	-1.515
$NiCr_2O_4$ (12, monoclinic)	76.9	Stable	-5.529	-1.888
$NiCr_2O_4$ (227, cubic)	Exp 37.04 [56] 40.7 [57]	Not stable	-5.550	-1.909
$NiCr_2O_4$ (9, monoclinic, inverse spinel)	N/A	Not stable	-5.547	-1.906
$NiCr_2O_4$ (46, orthorhombic, inverse spinel)	N/A	Not stable	-5.547	-1.906
$NiFe_2O_4$ (74, orthorhombic, inverse spinel)	Exp 70.6[58] 82.63 [59]	Not stable	-5.342	-1.408
$FeNi_2O_4$ (227, cubic)	60.3	Stable	-5.045	-1.128
$NiFe_2O_4$ (227, cubic)	47.7 [55]	Not stable	-5.140	-1.206

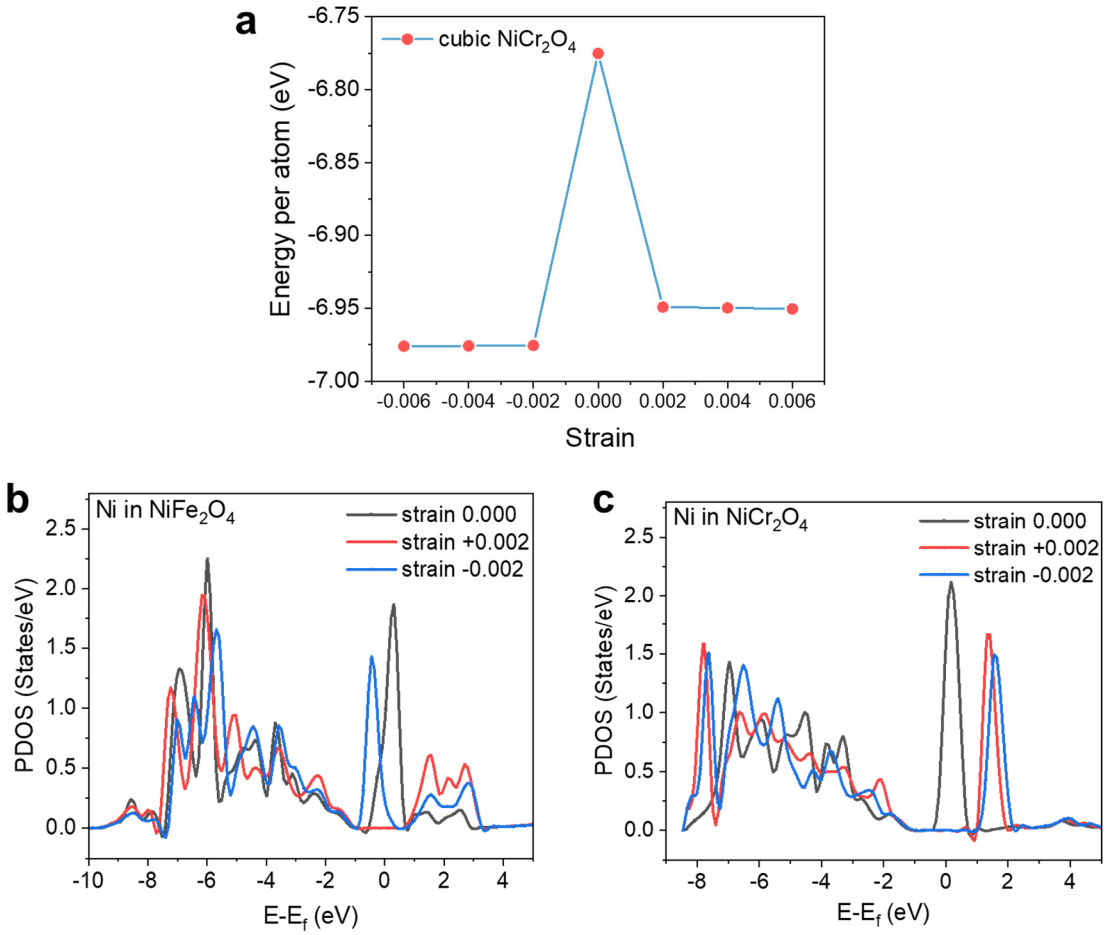

Supplementary Figure 35. Spinel structure formation energy from DFT calculations. a. Energy per atom for cubic $NiCr_2O_4$ spinel under different minor shear strain. Projected density of states (PDOS) for **b** Ni in $NiCr_2O_4$, and **c** Ni in $NiFe_2O_4$ at shear strain γ = -0.002, 0, +0.002 demonstrating the John-Teller effect.

References

1. García-León RA, Martínez-Trinidad J, Guevara-Morales A, Campos-Silva I, Figueroa-López U. Wear Maps and Statistical Approach of AISI 316L Alloy under Dry Sliding Conditions. *J Mater Eng Perform* **30**, 6175-6190 (2021).
2. Pei X, Du Y, Li T, Wang H, Hu M, Wang H. A combinatorial evaluation of TiZrV0.5Nb0.5Six refractory high entropy alloys: Microstructure, mechanical properties, wear and oxidation behaviors. *Materials Characterization* **201**, 112956 (2023).
3. Yang S, Gao S, Xue W, Wu B, Duan D. Structural design and high temperature tribological behavior of a new turbine blade tip protective coating. *Surface and Coatings Technology* **457**, 129316 (2023).
4. Sun B, Ding F, Qiu B, Zhao Y, Guo J. High temperature tribological properties of NiAl-Ag2Mo2O7 composite coatings prepared by spark plasma sintering. *Surface and Coatings Technology* **456**, 129290 (2023).
5. Hao E*, et al.* Effect of alloying elements on microstructure evolution and wear mechanism of MCrAlX-based coatings at 800 °C. *Surface and Coatings Technology* **456**, 129266 (2023).
6. Kong X, Sun W, Wang Q, Chen M, Zhang T, Wang F. Improving high-temperature wear resistance of NiCr matrix self-lubricating composites by controlling oxidation and surface texturing. *Journal of Materials Science & Technology* **131**, 253-263 (2022).
7. Sun S, Li L, Hu C, Li Q, Yuan T. Tribological Behavior of a Shot-Peened Nickel-Based Single Crystal Superalloy at High Temperature. *Tribol Lett* **70**, 100 (2022).
8. Li K, Liang J, Zhou J. Microstructure and elevated temperature tribological performance of the CoCrFeNiMo high entropy alloy coatings. *Surface and Coatings Technology* **449**, 128978 (2022).
9. Jin C, Li X, Li H, Li Q, Wang H. Tribological performance of a TiZrNbMo0.6 refractory high entropy alloy at elevated temperatures. *Journal of Alloys and Compounds* **920**, 165915 (2022).
10. Zhang M, Zhang X, Niu M, Jiang Z, Chen H, Sun Y. High-temperature tribological behavior of CoCrFeNiV high-entropy alloys: A parallel comparison with CoCrFeNiMn high-entropy alloys. *Tribology International* **174**, 107736 (2022).
11. Wang Y*, et al.* High temperature induced “glaze” layer formed in HVOF-sprayed NiCrWMoCuCBFe coating and its wear reduction mechanism. *Friction* **10**, 1424-1438 (2022).
12. Cheng Q*, et al.* Microstructure evolution and wear mechanism of in situ prepared Ti–TiN cermet layers at high temperature. *Composites Part B: Engineering* **242**, 110028 (2022).
13. Xin B, Zhang A, Han J, Meng J. The tribological properties of carbon doped Al0.2Co1.5CrFeNi1.5Ti0.5 high entropy alloys. *Wear* **484-485**, 204045 (2021).
14. Wang D*, et al.* Tribological properties of Ni3Al-Ni3Nb-Ag self-lubricating alloys at a wide temperature range. *Wear* **480-481**, 203933 (2021).
15. Attia MH, de Pannemaecker A, Williams G. Effect of temperature on tribo-oxide formation and the fretting wear and friction behavior of zirconium and nickel-based alloys. *Wear* **476**, 203722 (2021).
16. Koricherla MV, Torgerson TB, Alidokht SA, Munagala VNV, Chromik RR, Scharf TW. High temperature sliding wear behavior and mechanisms of cold-sprayed Ti and Ti–TiC composite coatings. *Wear* **476**, 203746 (2021).
17. Kong X, Liu Y, Chen M, Zhang T, Wang F. High Temperature Oxidation and Tribological Behaviors of NiCrAl-Graphite Self-Lubricating Composites. *Acta Metallurgica Sinica (English Letters)* **34**, 900-912 (2021).

18. Thasleem P, Kuriachen B, Kumar D, Ahmed A, Joy M. Effect of heat treatment and electric discharge alloying on the tribological performance of selective laser melted AlSi10Mg. *Journal of Tribology* **143**, 051111 (2021).
19. Rahman MS, Ding J, Beheshti A, Zhang X, Polycarpou AA. Elevated temperature tribology of Ni alloys under helium environment for nuclear reactor applications. *Tribology International* **123**, 372-384 (2018).
20. Shi P*, et al.* TiO2–ZnO/Ni–5wt.%Al composite coatings on GH4169 superalloys by atmospheric plasma spray techniques and theirs elevated-temperature tribological behavior. *Ceramics International* **46**, 13527-13538 (2020).
21. Wang W*, et al.* Microstructure, mechanical and tribological properties of Mo-V-N films by reactive magnetron sputtering. *Surface and Coatings Technology* **387**, 125532 (2020).
22. Sun W*, et al.* Tribological behavior of cold sprayed Inconel 718 coatings at room and elevated temperatures. *Surface and Coatings Technology* **385**, 125386 (2020).
23. Pan S, Zhao C, Zhu W, Jiang F, Zhou J, Ren F. Sliding Wear Behavior of Spark Plasma-Sintered Cu–6 Wt Pct Cr Alloy at Room and Elevated Temperatures. *Metallurgical and Materials Transactions A* **50**, 3132-3147 (2019).
24. Feng S, Zhou X, Zhang Q. Tribological Behavior of Ni-based Self-lubricating Composites with the Addition of Ti3SiC2 and Ag2W2O7. *Journal of Wuhan University of Technology-Mater Sci Ed* **34**, 698-706 (2019).
25. Dreano A, Fouvry S, Guillonneau G. A combined friction energy and tribo-oxidation formulation to describe the high temperature fretting wear response of a cobalt-based alloy. *Wear* **426-427**, 712-724 (2019).
26. Munagala VNV, Torgerson TB, Scharf TW, Chromik RR. High temperature friction and wear behavior of cold-sprayed Ti6Al4V and Ti6Al4V-TiC composite coatings. *Wear* **426-427**, 357-369 (2019).
27. Li X, Yin H, Li Y-F. Tribological Properties of Spark Plasma Sintered NiCr–Cr2AlC Composites at Elevated Temperature. *Journal of Tribology* **141**, 032202 (2019).
28. Chu K, Zhou J, Ren F. Sliding wear of nanocrystalline Nb-Ag at elevated temperatures: Evolution of subsurface microstructure and its correlation with wear performance. *Wear* **414-415**, 251-261 (2018).
29. Yang F, Su B, Zhang A, Meng J, Han J, Wu Y. Tribological properties and wear mechanisms of Mo2FeB2 based cermets at high temperatures. *Tribology International* **120**, 391-397 (2018).
30. Khajuria G, Wani MF. High-Temperature Friction and Wear Studies of Nimonic 80A and Nimonic 90 Against Nimonic 75 Under Dry Sliding Conditions. *Tribol Lett* **65**, 100 (2017).
31. Viat A, Dreano A, Fouvry S, De Barros Bouchet M-I, Henne J-F. Fretting wear of pure cobalt chromium and nickel to identify the distinct roles of HS25 alloying elements in high temperature glaze layer formation. *Wear* **376-377**, 1043-1054 (2017).
32. Li Y-F, Yin H, Li X-L, Mao C-C. Friction and Wear Properties of Spark Plasma Sintering NiCr–SrSO 4 Composites at Elevated Temperatures in Sliding Against Alumina Ball. *Tribol Lett* **64**, 1-10 (2016).
33. Wang J, Wang W, Jia J. The oxidation resistance and tribological properties of Ni-based composites with in situ/ex situ Al2O3 and TiC ceramic phases at high temperatures. *Journal of Materials Research* **31**, 3262-3271 (2016).
34. Qin Y*, et al.* Adaptive-lubricating PEO/Ag/MoS2 multilayered coatings for Ti6Al4V alloy at elevated temperature. *Materials & Design* **107**, 311-321 (2016).
35. Scharf TW, Prasad SV, Kotula PG, Michael JR, Robino CV. Elevated temperature tribology of cobalt and tantalum-based alloys. *Wear* **330-331**, 199-208 (2015).

36. Niu M, Bi Q, Zhu S, Yang J, Liu W. Microstructure, phase transition and tribological performances of Ni3Si-based self-lubricating composite coatings. *Journal of alloys and compounds* **555**, 367-374 (2013).
37. Ouyang J-H, Liang X-S, Liu Z-G, Yang Z-L, Wang Y-J. Friction and wear properties of hot-pressed NiCr–BaCr2O4 high temperature self-lubricating composites. *Wear* **301**, 820-827 (2013).
38. Li J, Xiong D. Tribological behavior of graphite-containing nickel-based composite as function of temperature, load and counterface. *Wear* **266**, 360-367 (2009).
39. Kashani H, Amadeh A, Ohadizadeh A. Effect of temperature on the strain induced γ→ε phase transformation in Stellite 21 during wear test. *Materials Science and Engineering: A* **435-436**, 474-477 (2006).
40. Stott FH, Jordan MP. The effects of load and substrate hardness on the development and maintenance of wear-protective layers during sliding at elevated temperatures. *Wear* **250**, 391-400 (2001).
41. Stott F, Lin D, Wood G, Stevenson C. The tribological behaviour of nickel and nickel-chromium alloys at temperatures from 20 to 800 C. *Wear* **36**, 147-174 (1976).
42. Lin D, Stott F, Wood G. The effects of elevated ambient temperatures on the friction and wear behavior of some commercial nickel base alloys. *ASLE TRANSACTIONS* **17**, 251-262 (1974).
43. Bak P, Tang C, Wiesenfeld K. Self-organized criticality: An explanation of the 1/f noise. *Physical review letters* **59**, 381 (1987).
44. Zypman FR, Ferrante J, Jansen M, Scanlon K, Abel P. Evidence of self-organized criticality in dry sliding friction. *Journal of Physics: Condensed Matter* **15**, L191 (2003).
45. Buldyrev SV, Ferrante J, Zypman FR. Dry friction avalanches: Experiment and theory. *Physical Review E* **74**, 066110 (2006).
46. Yu JW, Rahbari S, Kawasaki T, Park H, Lee WB. Active microrheology of a bulk metallic glass. *Science Advances* **6**, eaba8766 (2020).
47. Duarte M, Molina J, Prieto R, Louis E, Narciso J. Self-similar fluctuations and 1/f noise in dry friction dynamics. *Metallurgical and Materials Transactions A* **38**, 298-305 (2007).
48. Duarte M, Vragovic I, Molina J, Prieto R, Narciso J, Louis E. 1/f noise in sliding friction under wear conditions: The role of debris. *Physical review letters* **102**, 045501 (2009).
49. Stott F. The role of oxidation in the wear of alloys. *Tribology International* **31**, 61-71 (1998).
50. Archard JF. Contact and Rubbing of Flat Surfaces. *Journal of Applied Physics* **24**, 981-988 (1953).
51. Beake BD. The influence of the H/E ratio on wear resistance of coating systems – Insights from small-scale testing. *Surface and Coatings Technology* **442**, 128272 (2022).
52. Finkin EF. Examination of Abrasion Resistance Criteria for Some Ductile Metals. *Journal of Lubrication Technology* **96**, 210-214 (1974).
53. Wood G, Hodgkiess T. The hardness of oxides at ambient temperatures. *Materials and Corrosion* **23**, 766-773 (1972).
54. Liu Y, Xing J, Li Y, Tan J, Sun L, Yan J. Mechanical properties and anisotropy of thermal conductivity of Fe3–x Cr x O4 (x = 0–3). *Journal of Materials Research* **31**, 3805-3813 (2016).
55. Kim M, Kang J, Kim J, Kim J. Corrosion Protection Oxide Scale Formed on Surface of Fe-Ni-M (M = Al, Cr, Cu) Inert Anode for Molten Salt Electrolysis. *Materials* **15**, 719 (2022).
56. Hearmon R. The elastic constants of crystals and other anisotropic materials. *Landolt-Bornstein Tables, III/11* **1244**, (1979).
57. He L*, et al.* The anisotropic oxidation behavior of Hastelloy X alloy fabricated by laser powder-bed fusion (LPBF) during the cyclic oxidation process. *Corrosion Science* **217**, 111156 (2023).
58. Li Z, Fisher ES, Liu JZ, Nevitt MV. Single-crystal elastic constants of Co-Al and Co-Fe spinels. *Journal of Materials Science* **26**, 2621-2624 (1991).

59. Wangchhuk J, Meher SR. Structural, electronic and magnetic properties of inverse spinel NiFe2O4: DFT + U investigation. *Physics Letters A* **443**, 128202 (2022).